Monthly Notices
of the
ROYAL ASTRONOMICAL SOCIETY

MNRAS **489,** 2702–2722 (2019)
Advance Access publication 2019 August 29

doi:10.1093/mnras/stz2318

The impact of AGN on stellar kinematics and orbits in simulated massive galaxies

Matteo Frigo [1]★ Thorsten Naab,[1] Michaela Hirschmann,[2,3] Ena Choi,[4] Rachel S. Somerville,[5,6] Davor Krajnovic,[7] Romeel Davé [8,9] and Michele Cappellari [10]

[1]*Max-Planck-Institut fuer Astrophysik, Karl-Schwarzschild-Strasse 1, D-85741 Garching, Germany*
[2]*DARK, Niels Bohr Institute, University of Copenhagen, Lyngbyvej 2, 2100 Copenhagen, Denmark*
[3]*Institut d' Astrophysique de Paris, F-75014 Paris, France*
[4]*Department of Astronomy, Columbia University, New York, NY 10027, USA*
[5]*Center for Computational Astrophysics, Flatiron Institute, 162 5th Ave, New York, NY 10010, USA*
[6]*Department of Physics and Astronomy, Rutgers University, 136 Frelinghuysen Road, Piscataway, NJ 08854, USA*
[7]*Leibniz-Institut fur Astrophysik Potsdam (AIP), An der Sternwarte 16, D-14482 Potsdam, Germany*
[8]*Institute for Astronomy, University of Edinburgh, Royal Observatory, Edinburgh EH9 3HJ, UK*
[9]*Department of Physics and Astronomy, University of the Western Cape, Bellville, Cape Town 7535, South Africa*
[10]*Sub-Department of Astrophysics, Department of Physics, University of Oxford, Denys Wilkinson Building, Keble Road, Oxford OX1 3RH, UK*

Accepted 2019 August 19. Received 2019 August 12; in original form 2018 November 27

ABSTRACT

We present a series of 10 × 2 cosmological zoom simulations of the formation of massive galaxies with and without a model for active galactic nucleus (AGN) feedback. Differences in stellar population and kinematic properties are evaluated by constructing mock integral field unit maps. The impact of the AGN is weak at high redshift when all systems are mostly fast rotating and disc-like. After $z \sim 1$ the AGN simulations result in lower mass, older, less metal rich, and slower rotating systems with less discy isophotes – in general agreement with observations. 2D kinematic maps of *in situ* and accreted stars show that these differences result from reduced *in-situ* star formation due to AGN feedback. A full analysis of stellar orbits indicates that galaxies simulated with AGN are typically more triaxial and have higher fractions of x-tubes and box orbits and lower fractions of z-tubes. This trend can also be explained by reduced late *in-situ* star formation. We introduce a global parameter, ξ_3, to characterize the anticorrelation between the third-order kinematic moment h_3 and the line-of-sight velocity ($V_{\rm avg}/\sigma$), and compare to ATLAS^{3D} observations. The kinematic correlation parameter ξ_3 might be a useful diagnostic for large integral field surveys as it is a kinematic indicator for intrinsic shape and orbital content.

Key words: methods: numerical – galaxies: evolution – galaxies: formation – galaxies: kinematics and dynamics.

1 INTRODUCTION

The kinematics of stars within galaxies are a powerful tool to understand a galaxy's formation history. Since their dynamics are to good approximation collisionless (see Binney & Tremaine 1987), stars preserve information about their origin for a long time. Stars can either originate from the galaxy itself, forming *in situ* through the gravitational collapse of gas, or can get accreted from different galaxies during merger events. These two types of origin lead to different dynamical properties: newly *in-situ*-formed stars follow the dissipational dynamics of the gas which formed them, and this can lead to the formation of orderly rotating stellar discs (e.g. Robertson et al. 2004). The process of accreting stars from other galaxies is instead purely collisionless, and tends to result in round dispersion supported systems (e.g. Naab, Johansson & Ostriker 2009). Because of this connection, many studies attributed the difference in dynamical properties of present-day galaxies to different stellar origins. The more massive and bright early-type galaxies (with absolute magnitude $M_V \lesssim -21.5$), whose stellar component has been for a significant part accreted, tend to have smaller angular momentum (Emsellem et al. 2011) and more

★ E-mail: mfrigo@mpa-garching.mpg.de

© 2019 The Author(s)
Published by Oxford University Press on behalf of the Royal Astronomical Society

Downloaded from https://academic.oup.com/mnras/article-abstract/489/2/2702/5556548 by Said Business School user on 05 November 2019

complex kinematics (Krajnović et al. 2011), while intermediate and low-mass galaxies ($M_V \gtrsim -21.5$), which have formed most of their stars *in-situ*, tend to be simple, flattened, fast-rotating systems (see Cappellari 2016 for a review). Using cosmological simulations, Naab et al. (2014) and Röttgers, Naab & Oser (2014) linked the present-day kinematics of galaxies to the type of galaxy mergers they experienced during their formation: minor or major, and with or without gas. They found that gas-rich formation histories are more likely to produce fast-rotating systems, while gas-poor galaxy mergers tend to lead to slow-rotating systems. They however also found major mergers with particular configurations which result in an increase of the galactic angular momentum, displaying a complex picture. This picture would however be incomplete without including the energy feedback from active galactic nuclei (AGN). The connection between AGN and their host galaxies has been subject of research for more than two decades. Soon after the discovery of supermassive black holes (SMBH) in the centres of early-type galaxies, correlations have been found between their mass and galactic properties such as galactic bulge mass and velocity dispersion (Dressler 1989; Kormendy 1993; Gebhardt et al. 2000). This connection has been in the focus of theoretical work, with the conclusion that the energy feedback from accreting black holes could be necessary to reproduce these scaling relations, as well as to obtain the correct masses and abundances of early-type galaxies in cosmological simulations (see e.g. Di Matteo, Springel & Hernquist 2005; Croton et al. 2006; Vogelsberger et al. 2014; Schaye et al. 2015 and reviews by Kormendy & Ho 2013, Somerville & Davé 2015 and Naab & Ostriker 2017). The impact of AGN might also go beyond affecting global properties. The cosmological simulations of Choi et al. (2015, 2017) showed that in low-redshift galaxies the fraction of stars that form *in situ* is much lower when including AGN feedback. This has strong repercussions on the morphological and kinematic properties of the host galaxy. Dubois et al. (2016) and Penoyre et al. (2017a) showed that including AGN feedback in cosmological simulations increases the abundance of slow-rotating systems. Bryan et al. (2012) showed that AGN feedback affects the orbital composition of simulated galaxies up to large radii.

In this paper we analyse a small sample of high-resolution 'zoom' simulations (see Fig. 1) for a more in-depth look at the impact of AGN feedback on the kinematic and stellar-population properties of galaxies, but also extending the analysis to higher-order kinematics and orbital structure. We compare our simulated galaxies to observations by mocking the images produced by integral field unit (IFU) spectrographs. These instruments collect a spectrum for each of their spatial pixels, so that one can observe the spatial distribution of spectrum-derived quantities, such as line-of-sight velocity, metallicity, and age. Recently a number of large galaxy surveys have been performed with IFU spectrographs, such as MaNGA (Bundy et al. 2015), SAMI (Croom et al. 2012), and CALIFA (Sánchez et al. 2012), resulting in the mapping of thousands of galaxies. The MUSE spectrograph (Bacon et al. 2010) also delivered detailed 2D maps of galactic properties (e.g. Emsellem, Krajnović & Sarzi 2014; Krajnović et al. 2018), including at high redshift (Guérou et al. 2016). For the study of AGN feedback, this means that there is a huge library of data that can be used to look for signatures of the effect of AGNs, and in this paper we want to understand the nature of generic signatures through cosmological simulations. We do this by running each of our simulations twice, once with and once without our AGN feedback implementation, in order to find and analyse the differences between the two cases.

In Section 2 we present the set of cosmological simulations analysed in this paper. In Section 3 we describe how our mock observational maps are created, and how the other values we present are calculated. In Section 4 we look at the effect of AGN feedback on one exemplary simulated galaxy, through our mock integral field maps. In Section 5 we analyse the full simulation sample to get an idea of the general impact of AGN feedback. In Section 6 we discuss and summarize our conclusions.

2 SIMULATION DETAILS

2.1 Cosmological 'zoom' simulations

In this work we analyse a set of 20 prototypical cosmological *zoom* simulations of massive galaxies for the impact of feedback from accreting SMBH. Each of our 10 initial conditions is simulated once with and once without the AGN feedback model. Throughout the paper the two cases will be labelled as *AGN* and *NoAGN*. The initial conditions for the simulations were constructed from a $(100\,\mathrm{Mpc})^3$ dark matter only simulation with a *WMAP3* cosmology (Spergel et al. 2007): $h = 0.72$, $\Omega_\mathrm{b} = 0.044$, $\Omega_\mathrm{dm} = 0.216$, $\Omega_\Lambda = 0.74$, $\sigma_8 = 0.77$, $n_\mathrm{s} = 0.95$. All details on the construction of the zoom initial conditions are presented in Oser et al. (2010, 2012). The same initial conditions were used in e.g. Naab et al. 2014 and Hirschmann et al. 2012, 2013; Naab et al. 2014 and Hirschmann et al. 2017, but here we simulate at higher resolution. Dark matter particles have a mass of $m_p = 3.62 \times 10^6\,\mathrm{M}_\odot\,h^{-1}$ and gas particles initially have mass of $m_p = 7.37 \times 10^5\mathrm{M}_\odot\,h^{-1}$. The simulations are run from $z = 43$ to $z = 0$ with gravitational softening lengths of 0.2 kpc for gas, star, and black hole particles and 0.45 kpc for dark matter particles at the highest resolution level.

The simulation code is the same as the one used in Hirschmann et al. (2017). We used an improved version of GADGET-3 (Springel 2005), SPHGAL, which overcomes the numerical limitations of the classic smoothed particle hydrodynamics (SPH) implementation. All details of SPHGAL are given in Hu et al. (2014).

2.1.1 *Star formation and feedback*

The simulation code includes a model for the formation of stellar populations from gas particles, representing star formation and for feedback. The stellar populations provide thermal and kinetic feedback as well as metals to the interstellar medium. The chemical enrichment was originally described by Scannapieco et al. (2005, 2006) and later improved by Aumer et al. (2013) and Núñez et al. (2017) with an updated feedback model. Gas particles are stochastically converted into star particles depending on the density of the gas, in a way that reproduces the Kennicutt–Schmidt relation (Kennicutt 1998). To be eligible for conversion into stars, SPH particles need to have density higher than a threshold density value ρ_th, given by:

$$\rho_\mathrm{th} = \rho_0 \left(\frac{T_\mathrm{gas}}{T_0}\right)^3 \left(\frac{M_\mathrm{gas}}{M_0}\right)^{-2}, \quad (1)$$

where $\rho_0 = 1\,\mathrm{cm}^{-3}$, $M_0 = 1.3 \cdot 10^6\,\mathrm{M}_\odot$, $T_0 = 6000\,K$, and M_gas and T_gas are the mass and temperature of the gas particle, respectively (Núñez et al. 2017). In each time-step the eligible particles are assigned a probability of converting into star particles, so that the time-averaged star formation rate is:

$$\frac{\mathrm{d}\rho_\star}{\mathrm{d}t} = \epsilon_\mathrm{SFR}\,\frac{\rho_\mathrm{gas}}{t_\mathrm{dyn}}, \quad (2)$$

Downloaded from https://academic.oup.com/mnras/article-abstract/489/2/2702/5556548 by Said Business School user on 05 November 2019

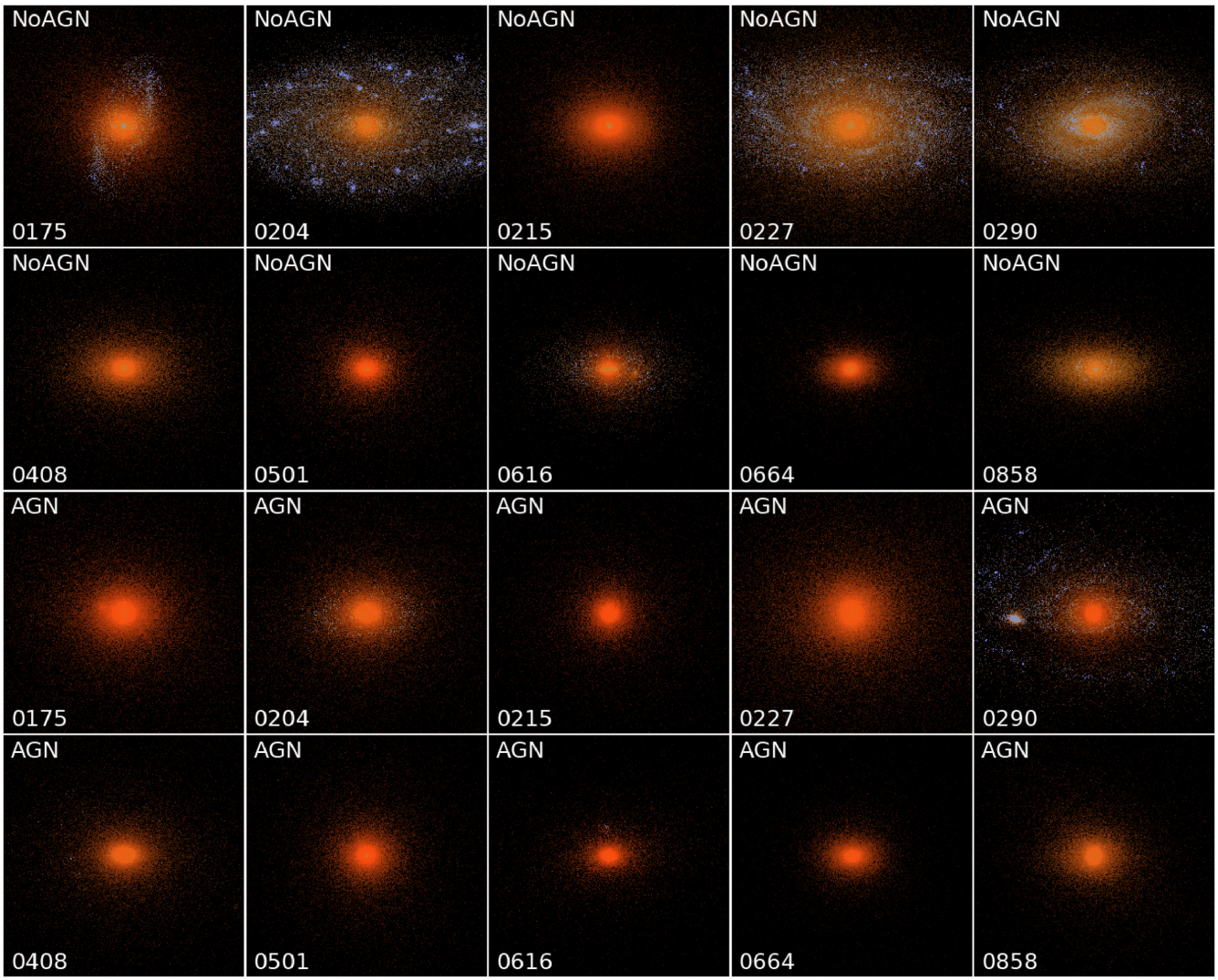

Figure 1. Mock luminosity images of our sample of simulated galaxies, run without (top two rows) and with (bottom two rows) AGN feedback. All galaxies are viewed at an inclination of 60 degrees (where 90 would mean edge-on). Stars are colour-coded by *V*-band weighted age based on Bruzual & Charlot (2003). Several of the galaxies simulated without AGN feedback show the presence of young stellar discs, which is unusual for galaxies of this mass.

where $t_{\rm dyn} = \sqrt{4\,\pi\,G\,\rho_{\rm gas}}$ is the dynamical time of the gas particle and $\epsilon_{\rm SFR} = 0.025$ is the star formation efficiency (chosen as in Núñez et al. 2017 and Hirschmann et al. 2017). The newly created star particles are then treated as collisionless. Each particle represents a single stellar population assuming a Kroupa (2001) initial mass function, with a given age and the metallicity of the original gas particle. This stellar population then exerts feedback to the surrounding gas. This takes the form of type Ia and II supernovae and of winds from asymptotic giant branch (AGB) stars. Type II supernovae happen at a given time $\tau_{\rm SNII} = 3\,$Myr after the creation of the star particles. This is on the short end of the typical delay time distributions for type II supernovae. Type Ia supernovae and AGB winds are added every 50 Myr after the star particle creation. Each event provides momentum and thermal energy to the surrounding gas. The total feedback energy is given by:

$$E = \frac{1}{2}\, m_{\rm ejected}\, v_{\rm out}^2, \tag{3}$$

where $m_{\rm ejected}$ is the mass ejected by the stellar population and $v_{\rm out}$ is the assumed ejecta velocity. These are determined depending on the mass, age, and metallicity of the particle and on the type of event. We assume $v_{\rm out} = 4500\,{\rm km\,s^{-1}}$ for type Ia and type II supernovae and $v_{\rm out} = 10\,{\rm km\,s^{-1}}$ for AGB stars. The ejecta mass is taken from Woosley & Weaver (1995) for type II and from Iwamoto et al. (1999) for type Ia supernovae. This energy and mass is then added to the surrounding gas both as thermal (heating) and as momentum feedback (pushing). The relative fraction depends on the density and distance between the supernova-undergoing stellar particle and the 10 neighbouring gas particles, mimicking the evolution of blast waves (a simplified version of the three-phase model adopted in Núñez et al. 2017; see Hirschmann et al. 2017). The feedback events also distribute metals to the surrounding gas. Eleven elements are tracked for every gas and star particle (H, He, C, N, O, Ne, Mg, Si, S, Ca, and Fe), and their abundances are used to compute the cooling rate of the gas with the yields from Karakas (2010), Iwamoto et al. (1999), and Woosley & Weaver (1995) for AGB winds and supernovae type Ia and II, respectively. All details can be found in Aumer et al. (2013), Aumer, White & Naab (2014), and Núñez et al. (2017).

Downloaded from https://academic.oup.com/mnras/article-abstract/489/2/2702/5556548 by Said Business School user on 05 November 2019

2.1.2 AGN feedback

AGN feedback is represented through the model developed by Choi et al. (2012) and used in Choi et al. (2014, 2015, 2017). This model includes both a radiative and a kinetic (wind) component (see Naab & Ostriker 2017 for a discussion of alternative numerical implementations). While it does not explicitly include relativistic jets, this model has been proven to produce galaxies with realistic sizes, star formation rates, black hole mass relations, and in particular hot gas (X-ray) properties without separating into different feedback modes (Choi et al. 2012, 2014, 2015, 2017; Eisenreich et al. 2017; Choi et al. 2018).

Here we summarize the most important elements used for this study. Black holes are first seeded at the centre of haloes exceeding a mass of $10^{11}\,\mathrm{M}_{\odot}$, with an initial mass of $M_{\mathrm{BH}} = 10^{5}\,\mathrm{M}_{\odot}$, and they are repositioned on the potential minimum of their host galaxy at every time-step. They can then grow either by merging with other black hole particles or by accreting neighbouring gas particles according to a modified Bondi–Hoyle–Lyttleton (Hoyle & Lyttleton 1939; Bondi & Hoyle 1944; Bondi 1952) accretion rate:

$$\dot{M}_{\mathrm{BHL}} = \left\langle \frac{4\,\pi\,G^2\,M_{\mathrm{BH}}^2\,\rho}{(c_s^2 + v^2)^{3/2}} \right\rangle, \tag{4}$$

where M_{BH} is the mass of the supermassive black hole, and ρ, c_s, and v are the gas density, speed of sound and velocity with respect to the black hole. The calculation is done on an individual particle basis and then averaged over the SPH kernel, which is denoted by the angle brackets. This reduces the dependency on the number of SPH particles (see Choi et al. 2012). We do not explicitly enforce an Eddington limit cap on the accretion rate, as it is self-regulated by the inclusion of the Eddington force. We also do not add a 'boost' factor α (see Choi et al. 2017). Of the gas particles which could be accreted, 90 per cent are re-emitted as a wind parallel to the angular momentum of the gas next to the black hole (see Ostriker et al. 2010). This simulates the broad-line winds commonly emitted by AGN (de Kool et al. 2001; Somerville & Davé 2015; Naab & Ostriker 2017). The remaining 10 per cent are accreted, increasing the mass of the black hole particle. The model also includes radiative feedback in two forms. There is an Eddington radiation pressure force, which depends on the accretion rate and represents low energy photons providing momentum to the gas isotropically. We are also representing the higher energy X-ray photons, using the formulae from Sazonov et al. (2005) for Compton scattering. This component provides both momentum and thermal energy to the gas. As in Hirschmann et al. (2017), our simulation code differs from the one used in Choi et al. (2017) in not including metallicity-dependent heating, which was shown to have negligible impact (Choi et al. 2017).

3 ANALYSIS METHODS

3.1 Voronoi-binned kinematic maps

We study our simulations by analysing a series of mock IFU maps (e.g. Cappellari et al. 2011a) of the kinematics, metallicities, and ages of the stellar populations of the simulated galaxies. These maps are constructed with a PYTHON code developed for this work, following the analysis presented in Jesseit et al. (2007, 2009), Röttgers et al. (2014), and Naab et al. (2014). The code is included in the publicly available PYGAD analysis package.[1] Positions and velocities of the simulated galaxies are centred on the densest nuclear regions using a shrinking sphere technique on the stellar component. In the *AGN* simulations we centre the galaxies on their central supermassive black hole particles, which we define as the most massive black hole particle within 1 kpc of the stellar density centre. We then calculate the eigenvectors of the reduced inertia tensor (Bailin & Steinmetz 2005) of all stellar particles within 10 per cent of the virial radius R_{vir}, and use them to align the galaxies' principal axes with the coordinate systems, such that the x-axis is the long axis and the z-axis is the short axis. To mimic seeing effects, each star particle in the simulation is split into 60 'pseudoparticles', which keep the same velocity as the original particle and the positions are distributed according to a Gaussian with $\sigma = 0.2$ kpc centred on the original position of the particle (see Naab et al. 2014). In projection, the pseudoparticles are mapped on to a regular 2D grid, with pixel size 0.1 kpc (at $z = 0$). Adjacent bins of this grid are then joined so that each resulting spaxel has a similar signal-to-noise ratio. We do this using the Voronoi tessellation method presented in Cappellari & Copin (2003). For the maps presented in this paper, the target signal-to-noise level of the spaxels has been set such that each of them contains 25 000 pseudoparticles (∼400 regular particles). This ensures good statistics and results in maps similar to the ones from modern integral field surveys. The Voronoi grid is then used to construct the plots of stellar kinematics, metallicity, and age shown in this paper. For the age and metallicity maps, the value of every spaxel is calculated through a mass-weighted sample average. For the kinematic maps, we construct a histogram of the line-of-sight (LOS) velocity distribution of each spaxel, with the bin size determined by the Freedman & Diaconis (1981) rule. We then follow the classic approach of van der Marel & Franx (1993), Gerhard (1993), and fit the LOS velocity histogram with a Gauss–Hermite function:

$$f(V) = I_0\,e^{-y^2/2}(1 + h_3\,H_3(y) + h_4\,H_4(y)), \tag{5}$$

where $y = (V - V_{\mathrm{avg}})/\sigma$ and H_3 and H_4 are the Hermite polynomials of third and fourth order:

$$H_3(y) = (2\sqrt{2}\,y^3 - 3\sqrt{2}\,y)/\sqrt{6} \tag{6}$$

$$H_4(y) = (4\,y^4 - 12\,y^2 + 3)/\sqrt{24}. \tag{7}$$

The four fitting parameters V_{avg} (average velocity), σ (velocity dispersion), h_3 (skewness of the distribution), and h_4 (kurtosis of the distribution) are the ones plotted in the four panels of the kinematic maps.

To characterize the specific angular momentum of our galaxies we also employ the dimensionless λ_R parameter (Emsellem et al. 2007), defined as:

$$\lambda_R = \frac{\sum_i F_i R_i |V_i|}{\sum_i F_i R_i \sqrt{V_i^2 + \sigma_i^2}}, \tag{8}$$

where the sum has been carried out over the spaxels of the kinematic maps, and F_i, R_i, V_i, and σ_i are the flux, projected radius, average LOS velocity, and velocity dispersion of each spaxel, respectively. By limiting the sum to bins within a certain radius R, it is also possible to evaluate the cumulative radial λ_R profile for every galaxy. The values given in the tables and kinematic maps are all calculated within the projected half-mass radius R_{e}.

[1] https://bitbucket.org/broett/pygad

Downloaded from https://academic.oup.com/mnras/article-abstract/489/2/2702/5556548 by Said Business School user on 05 November 2019

3.2 Higher order kinematics

The higher order moments of the LOS velocity distribution, h_3 and h_4, can provide additional information on the orbital structure of our galaxies. In rotating systems the h_3 parameter has been observed to be anticorrelated to the average LOS velocity $V_{\rm avg}$, or more specifically to the $V_{\rm avg}/\sigma$ ratio (Gerhard 1993; Krajnović et al. 2011; van de Sande et al. 2017; Veale et al. 2017). This anticorrelation indicates that the LOS velocity distributions typically have a steep leading wing and a broad trailing wing. Simple axisymmetric rotating stellar systems show this property due to projection effects – stars are typically on circular orbits and those with lower LOS velocities projected into each spaxel produce a broad trailing wing. The slope of this anticorrelation is then about ∼0.1 (Bender, Saglia & Gerhard 1994). However, if the galaxy is more complex, i.e not axisymmetric, it can also contain stars orbiting around different axes or radial orbits. This can make the trailing wing broader, as these stars have lower LOS velocities. The slope of the anticorrelation would then be steeper, and in some slow-rotating galaxies it can become extremely steep (see e.g. van de Sande et al. 2017). If the group of rotating stars becomes subdominant the correlation between h_3 and $V_{\rm avg}/\sigma$ can change sign and become positive. Here the few fast rotating stars create a broad leading wing in the LOS velocity distribution (Naab, Jesseit & Burkert 2006; Hoffman et al. 2009; Röttgers et al. 2014). This unusual property is typically seen in simulated gas-poor mergers (Naab & Burkert 2001; Naab et al. 2014).

We characterize this variety of behaviours with a global parameter indicating the slope of the relation between h_3 and $V_{\rm avg}$ / σ for all spaxels of one galaxy. This definition is inspired by the finding in Naab et al. (2014) that different slopes indicate varying formation histories and by the improved empirical classifications of the SAMI and MASSIVE galaxy surveys (van de Sande et al. 2017; Veale et al. 2017). We define the kinematic correlation parameter ξ_3 as:

$$\xi_3 = \frac{\langle h_3\, V_{\rm avg}/\sigma\rangle}{\langle {h_3}^2\rangle} = \frac{\sum_i F_i\, h_{3,i}\, (V_i/\sigma_i)}{\sum_i F_i\, {h_{3,i}}^2}, \quad (9)$$

where the sum is calculated over each spaxel out to $R_{\rm e}$ from the centre, and the angle brackets indicate flux-weighted averaging over spaxels. When h_3 and $V_{\rm avg}/\sigma$ are correlated, this parameter estimates the inverse of the slope of the correlation to reasonable accuracy with a simple fraction of weighted sums; negative values indicate a negative correlation, while positive values indicate a positive one. This can be seen by assuming $\langle h_3\rangle = 0$ and $\langle V_{\rm avg}/\sigma\rangle = 0$ (which is justified if the kinematic maps are symmetric) and rewriting the definition of the parameter as:

$$\xi_3 = \rho_{V/\sigma,h_3}\, \frac{\sigma_{V/\sigma}}{\sigma_{h_3}}, \quad (10)$$

where $\rho_{V/\sigma,h_3}$ is the Pearson correlation coefficient of $V_{\rm avg}/\sigma$ and h_3, and $\sigma_{V/\sigma}$ and σ_{h_3} are the dispersion values of the two parameters (all flux-weighted). If h_3 and $V_{\rm avg}/\sigma$ are linearly correlated then $\rho = \pm 1$, and ξ_3 becomes exactly the slope of the correlation.

Fig. 2 shows an example of the $h_3 - V_{\rm avg}/\sigma$ spaxel values within $R_{\rm e}$ for four simulated galaxies with different LOS velocity distribution properties. The lines indicate the simple slope given by $h_3 = (1/\xi_3) \cdot V_{\rm avg}/\sigma$. Purely rotating systems are expected to have $\xi_3 \sim -10$, while rotating systems with non-negligible fractions of different orbit types are expected to lie in the $-3 < \xi_3 < -6$ range. When there is no correlation, or when the slope is almost vertical (both of which are observed in slow-rotating galaxies), the value of ξ_3 comes close to zero. Because of this, ξ_3 can potentially be a good way of distinguishing different types of galaxies. van de Sande et al. (2017) have used best-fitting elliptical Gaussians with a maximum likelihood approach to characterize the slope of the relation, which is slightly more complicated than our procedure. Veale et al. (2017) perform linear least-squares fit to calculate the slopes directly. Using the inverse of the slopes highlights the difference between slow rotators and the slow rotators get values around zero. The h_4 parameter is known to relate to orbit anisotropy (Gerhard 1993; van der Marel & Franx 1993; Thomas et al. 2007), with negative values indicating the dominance of tangential orbits and positive values corresponding to radial orbits. We do not further analyse h_4 other than showing the projected maps.

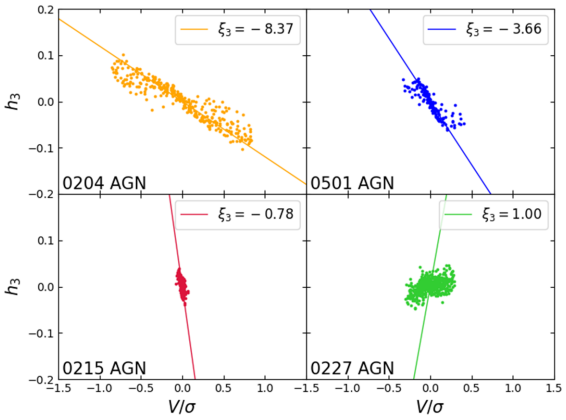

Figure 2. Four simulation examples for the relation between h_3 and $V_{\rm avg}/\sigma$ for the Voronoi bin within $R_{\rm e}$ with the corresponding ξ_3 values. The lines indicate $h_3 = (1/\xi_3) \cdot V_{\rm avg}/\sigma$. The upper left-hand panel shows a typical axisymmetric fast-rotator (0204 *AGN*), with a large fraction of prograde z-tube orbits ($f^{\rm pro}_{\rm z\text{-}tube} = 60$ per cent). It has the most negative ξ_3 value. The more complex fast-rotator 0501 *AGN* (upper right-hand panel, $f^{\rm pro}_{\rm z\text{-}tube} = 26$ per cent) shows a steeper slope with a higher ξ_3. Slow rotators like 0215 *AGN* (bottom left-hand panel, $f^{\rm pro}_{\rm z\text{-}tube} = 13$ per cent) have ξ_3 close to zero. Unusual non-axisymmetric rotating systems like 0227 *AGN* ($f^{\rm pro}_{\rm z\text{-}tube} = 20$ per cent) have a weak positive correlation between h_3 and $V_{\rm avg}/\sigma$ resulting in a slightly positive value of ξ_3 (bottom right-hand panel).

3.3 Isophotal shape and triaxiality

Our analysis involves the calculation of photometric quantities, such as the ellipticity ϵ and the isophotal shape parameter a_4/a, using stellar mass as a proxy for stellar light. The ellipticity values are calculated by fitting the galaxy isophotes with ellipses. The isophotes are constructed as lines with constant stellar surface mass density. For each galaxy we use 10 isophotes between $0.25R_{\rm e}$ and $R_{\rm e}$ and average their ellipticity values to obtain ϵ. The a_4/a parameter represents the deviation of the shape of the isophotes of the galaxy from a perfect ellipse. It is used to discriminate between galaxies with 'boxy' or 'discy' isophotes (Lauer 1985; Bender & Moellenhoff 1987). We calculate it by applying a Fourier expansion to the deviation of the actual isophotes from their best-fitting ellipse:

$$\delta\, R(\theta) = R(\theta) - R_{ell}(\theta) = \sum_n (a_n\, \cos(n\,\theta) + b_n\, \sin(n\,\theta)), \quad (11)$$

where θ is the azimuthal angle (Jedrzejewski 1987). The first-, second-, and third-order coefficients are negligible if the ellipse is centred correctly and has the correct ellipticity and orientation angle. The fourth-order coefficient a_4, normalized to the zeroth coefficient a, represents the deviation of the isophote from a pure ellipse. A positive value of a_4/a means that there is an excess of light along

Downloaded from https://academic.oup.com/mnras/article-abstract/489/2/2702/5556548 by Said Business School user on 05 November 2019

the major axis of the ellipse, causing the real isophote to be more 'discy'. A negative value instead means that the shape of the real isophote is more 'boxy' (see e.g. Naab, Burkert & Hernquist 1999; Springel 2000).

We also look at the 3D shape of our galaxies by computing the triaxiality parameter:

$$T = \frac{1-(b/a)^2}{1-(c/a)^2}, \tag{12}$$

where b/a and c/a are the ratios between the main axes. When $T = 0$ the galaxy is perfectly oblate, while when $T = 1$ the galaxy is perfectly prolate. We calculated the axis ratios through the reduced inertia tensor (Bailin & Steinmetz 2005) of all particles within the effective radius R_e:

$$\tilde{I}_{i,j} = \sum_{\text{Particles } k} m_k \frac{r_{k,i}\, r_{k,j}}{r_k^2}, \tag{13}$$

where m_k and $\vec{r}_k$ are the masses and positions of the particles. If the eigenvalues of $I_{i,j}$ are $\tilde{a}^2 > \tilde{b}^2 > \tilde{c}^2$, the ratios of their square roots $\tilde{b}/\tilde{a}$, $\tilde{c}/\tilde{a}$ are related to the real axis ratios by:

$$b/a = (\tilde{b}/\tilde{a})^{\sqrt{3}} \quad \text{and} \quad c/a = (\tilde{c}/\tilde{a})^{\sqrt{3}}. \tag{14}$$

The $\sqrt{3}$ exponent is an empirical fit accounting for the bias of the axis ratios towards unity due to measuring the reduced inertia tensor within a sphere (Bailin & Steinmetz 2005).

3.4 Orbit analysis

We analyse the orbital composition of each of our simulated galaxies following the approach of Jesseit, Naab & Burkert (2005) and Röttgers et al. (2014). This procedure starts by freezing the potential of the simulated galaxy at $z = 0$ and representing it analytically using the self-consistent field (SCF) method (Hernquist & Ostriker 1992): the density and potential are expressed as a sum of bi-orthogonal basis functions, which satisfy the Poisson equation. There are such multiple density-potential pairs (e.g. Vasiliev 2013 and Lilley et al. 2018). We used the one from Hernquist & Ostriker (1992), in which the zeroeth-order element is the Hernquist (1990) profile:

$$\rho_{000} = \frac{M}{2\pi a^3} \frac{1}{\frac{r}{a}\left(1+\frac{r}{a}\right)^3} \tag{15}$$

$$\Phi_{000} = -\frac{G M}{r+a}, \tag{16}$$

where a is the scale parameter of the Hernquist profile. Higher order terms then account for both radial and angular deviations. The maximum radial and angular orders are $n_{\max} = 18$ and $l_{\max} = 7$, respectively. In the AGN simulations, the central SMBH are represented with a point mass (with the same softening length as the original simulations), which is a simplier and more precise representation. This point mass potential is summed to the SCF potential calculated with all the other particles.

We then integrate the orbits of each stellar particle within this fixed analytical potential for about 50 orbital periods. This is enough for identifying the orbit type, but not so much that quasi-regular orbits diverge from regular phase-space regions forcing us to classify them as irregular. The integration is done with an eigth-order Runge–Kutta integrator. The orbit classification itself is then done using the code by Carpintero & Aguilar (1998), which distinguishes different orbit families by looking for resonances between their frequencies along different axes (up to $m < 29$, $n < 10$, if m: n is the resonance).

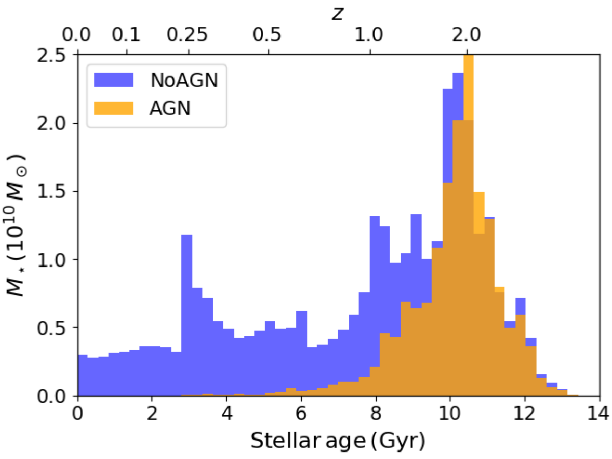

Figure 3. Age distribution of star particles in the case study galaxy (0227) for the run with AGN feedback (orange) and the one without (blue). The top x-axis shows the corresponding redshift at which the stars have formed. Star formation proceeded at a similar rate up $z = 2$. Then it is rapidly terminated in the presence of AGN feedback. Without AGN feedback star formation continues all the way to $z = 0$.

In this paper we consider three main families of orbits: z-tubes (orbits that rotate around the z axis), x-tubes (orbits that rotate around the x-axis), box orbits (π boxes and boxlets), and irregular orbits. In addition to these, we computed the fraction of prograde z-tube orbits $f^{\text{pro}}_{\text{z-tube}}$, by only selecting z-tubes with angular momentum along the z-axis of the same sign as the overall galaxy. Our orbit classification scheme makes sure that the orbit type of each particle is solid by analysing three different sections of the integrated orbit independently. If the three segments are classified differently, then we consider the classification to have failed, and we exclude these particles from the analysis (but they are still counted for computing the fraction of the other orbit types).

4 A TYPICAL GALAXY SIMULATED WITH AND WITHOUT AGN FEEDBACK

Our study involves a small sample of 20 massive galaxies. As a test case, in this section, we first discuss the formation history, global galaxy properties, stellar kinematics, stellar age and metallicity, morphology, and redshift evolution for one prototypical galaxy.

4.1 Formation history and global properties

Galaxy 0227 is an early-type galaxy, with an effective radius of 4.0 kpc and a stellar mass of 2×10^{11} $M_\odot$ in the *AGN* case and 5×10^{11} $M_\odot$ in the *NoAGN* case. Its formation history is characterized by a major merger at redshift $z \sim 0.25$, with mass ratio of 1: 1.7 and 1: 1.2 in the *NoAGN* and *AGN* cases. The presence of AGN has a strong influence on the evolution after the merger. Fig. 1 shows a mock *V*-band image of this galaxy with and without AGN feedback. In the absence of AGN feedback (left-hand panel) the galaxy is still forming new stars in an extended disc. Instead, in the case with AGN feedback (right-hand panel) the system is spheroidal with a very old stellar population.

Fig. 3 shows the age distribution of stars in galaxy 0227 simulated with and without AGN feedback. The oldest stars (age > 10 Gyr) have very similar age distributions, with the bulk forming around $z \sim 2$. Towards lower redshifts, star formation gets quenched in the *AGN* case; a behaviour found in all our simulations. While in the

Downloaded from https://academic.oup.com/mnras/article-abstract/489/2/2702/5556548 by Said Business School user on 05 November 2019

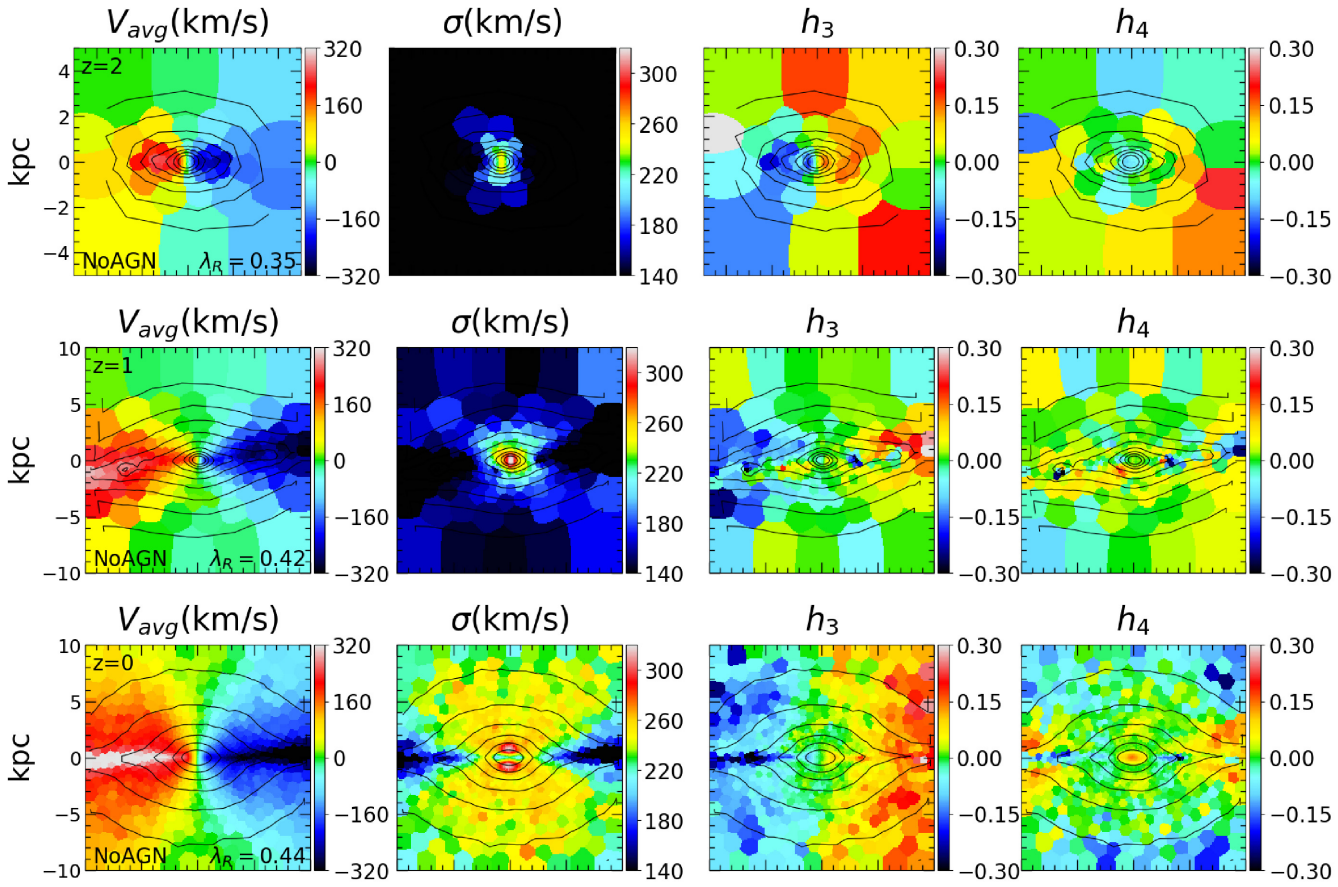

Figure 4. Edge-on 2D line-of-sight stellar kinematics (V_{avg}-σ-h_3-h_4 from left to right) of galaxy 0227 simulated without AGN feedback at $z = 2$, $z = 1$, and $z = 0$ (from top to bottom). The maps show typical features of systems with a disc-like component: high LOS velocity in the mid-plane, dumb-bell shaped velocity dispersion with a suppression in the mid-plane disc region, anticorrelation of line-of-sight velocity, and h_3 negative h_4 along the disc. These features become strongest at $z = 0$, when the disc is most prominent and can clearly be seen in the surface density contours (black lines).

AGN case not many stars form after $z \sim 1$, in the *NoAGN* case star formation continues throughout the simulation, including a starburst at $z \sim 0.25$ during the major merger.

4.2 LOS kinematics

In order to identify features in the stellar kinematics originating from the impact of AGN feedback, we construct 2D maps visualizing kinematic properties, as detailed in Section 3.1. Specifically we show the stellar line-of-sight velocity, dispersion, and the higher order moments h_3 and h_4 in Figs 4 and 5 for galaxy 0227 without and with AGN feedback at $z = 2$, $z = 1$, and $z = 0$. Initially (at $z = 2$ and $z = 1$) there are only moderate differences between the *AGN* and *NoAGN* simulations. The *AGN* and *NoAGN* galaxies (in brackets) have similar stellar masses of $M_* = 0.59 \times 10^{11}\,\mathrm{M}_\odot$ ($M_* = 0.54 \times 10^{11}\,\mathrm{M}_\odot$) at $z = 2$, while at $z = 1$ they are $M_* \sim 1.16 \times 10^{11}\,\mathrm{M}_\odot$ ($M_* \sim 1.97 \times 10^{11}\,\mathrm{M}_\odot$). The effective radii are $\sim$0.18 kpc ($\sim$0.35 kpc) at $z = 2$ and 0.95 kpc (1.53 kpc) at $z = 1$. Down to $z = 1$, the galaxies are supported by rotation. The average stellar line-of-sight velocities reach values of $\sim$200 km s^{-1}, and the velocity dispersion values around 300 km s^{-1}. The velocity increases only slightly from $z = 2$ to $z = 1$, but the rotating component becomes more extended for both cases. The h_3 parameter is anticorrelated with the LOS velocity – a typical signature for axisymmetric rotating systems (Krajnović et al. 2011; Naab et al. 2014). The origin of this effect is explained in detail in Section 3.2, as well as in Naab & Burkert (2001), Naab et al. (2006), Röttgers et al. (2014), and Naab et al. (2014) in the context of idealized models, merger simulations, and cosmological simulations. At redshift $z = 0$, the situation is markedly different. In the *NoAGN* case the rotation signatures are significantly enhanced. The LOS velocities reach up to 320 km s^{-1} in an extended disc. The velocity dispersion map shows a dumbbell feature with reduced velocity dispersion in the mid-plane, which is a signature of an edge-on rotation-supported disc embedded in a dispersion-supported spheroidal component. This can be seen by the isophotes (see Section 4.4). The LOS velocity distribution is asymmetric with anticorrelated h_3 values. The h_4 map shows characteristic features of disc rotation (bottom right-hand panel of Fig. 4). In the central kpc region, h_4 is positive, indicating a more peaked LOS velocity distribution with extended wings towards velocities lower and higher than the systemic velocity, as individual pixels cover significant fractions of the stars' orbits. At larger radii (in the mid-plane), h_4 becomes negative indicating coherent rotation with very weak tails towards high and low velocities. As h_4 is known to roughly correlate with the velocity anisotropy (Gerhard 1993; Thomas et al. 2007), a negative h_4 indicates that tangentially biased orbits are dominating, which is to be expected in a rotating disc. Kinematic maps of this kind are regularly found in observational surveys like ATLAS^{3D} (Cappellari et al. 2011b), CALIFA (Sánchez et al. 2012), or SAMI (Croom

Downloaded from https://academic.oup.com/mnras/article-abstract/489/2/2702/5556548 by Said Business School user on 05 November 2019

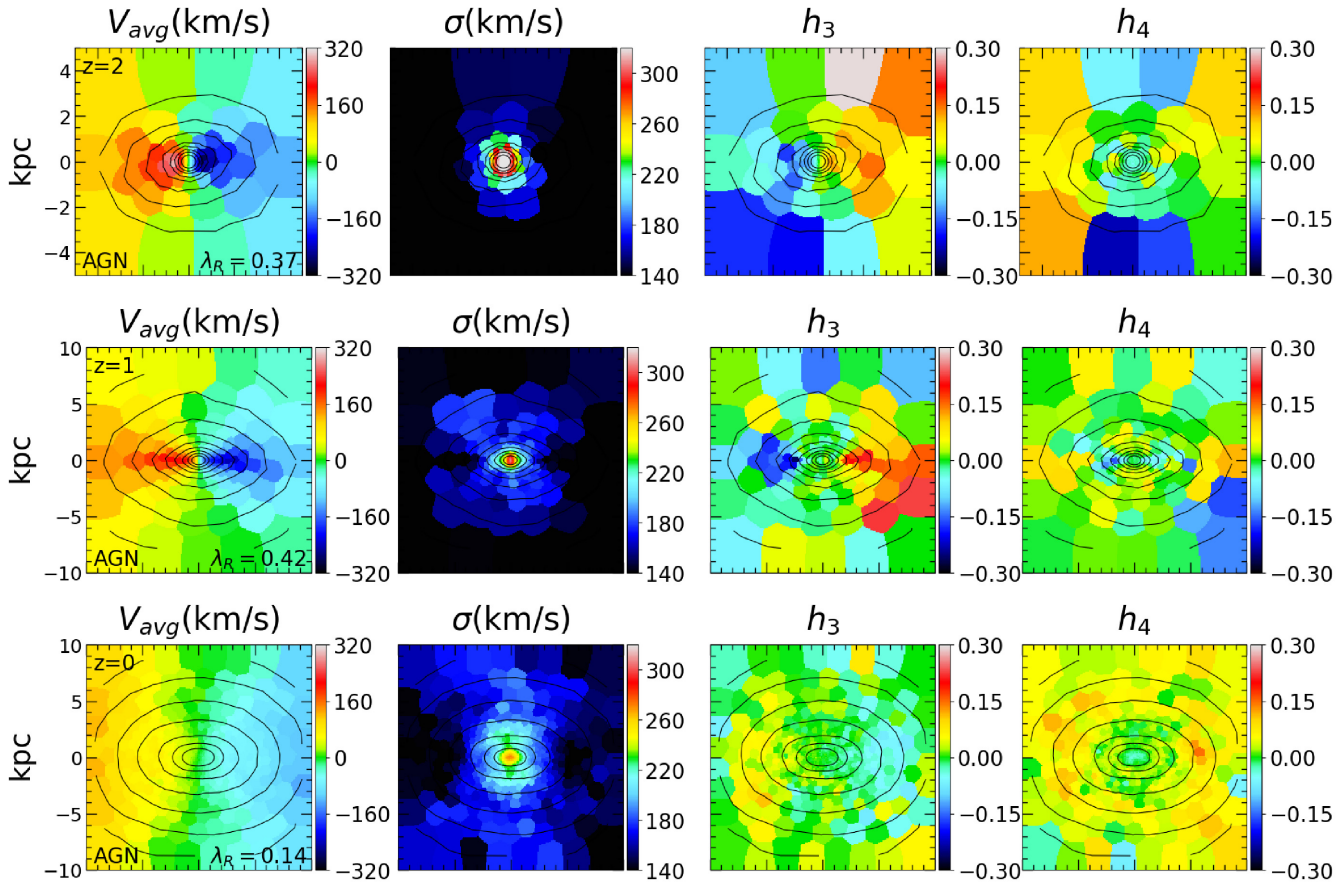

Figure 5. Same as Fig. 4 for galaxy 0227 simulated including AGN feedback. The kinematics is qualitatively similar to the case without AGN at $z = 2$ and $z = 1$. By $z = 0$ however the strong rotational signatures are gone, and the galaxy looks more like a typical slow-rotator without kinematic disc signatures: low average LOS velocity, high velocity dispersion, no h_3 anticorrelation signal, positive h_4.

et al. 2012). They are, however, more common for less massive galaxies. It is very unlikely to observe an elliptical galaxy of this high mass with such a prominent fast-rotating disc. The kinematic galaxy properties are very different in the *AGN* case (Fig. 5). By $z = 0$, there are no signatures of a prominent rotating stellar disc, as the AGN feedback prevents further gas accretion and *in-situ* disc formation (see e.g. Brennan et al. 2018). The galaxy is slowly rotating at $\sim$80 km s^{-1} and dispersion dominated, with only weak features in the higher order moments. Interestingly, h_3 is positively correlated with $V_{\rm avg}$ in the central part of the galaxy. This is rare for observed galaxies, but relatively common in the simulated remnants of gas-poor mergers (see Naab & Burkert 2001; Naab et al. 2006; Röttgers et al. 2014). This positive correlation must originate from a particular orbital distribution, which will be analysed in Section 4.6. Also a core with negative h_4 is still visible. Values for h_4 are positive in most of the map indicating radially biased orbits. All of the above features are typical properties of massive early-type galaxies.

4.3 Age and metallicity distribution at z = 0

Fig. 6 shows a comparison of the projected stellar age (top panels) and metallicity (bottom panels) distributions for the *NoAGN* (left-hand column) and *AGN* (right-hand column) simulation at $z = 0$. At low redshifts the properties of the systems differ the most. In the *NoAGN* case there is a distinct young $\lesssim$4 Gyr stellar disc embedded in an older 7–9 Gyr stellar bulge. A moderate positive age gradient towards younger ages away from the centre is visible. The disc appears as a flattened metal-enriched region in the mid-plane, pretty much following the isophotes. These features indicate ongoing disc-like star formation and metal enrichment since $z = 1$. This is also consistent with the stellar age distribution in Fig. 3. In the *AGN* case (right-hand panels of Fig. 6) the stellar population is older ($\sim$10 Gyr, see also Fig. 3), less metal enriched – due to less ongoing star formation – with a shallower metallicity gradient. There is a mild positive age gradient with younger ages in the centre caused by residual nuclear star formation. The origin of age and metallicity gradients will not be discussed further in this paper (see e.g. Hirschmann et al. 2015; Rodriguez-Gomez et al. 2016).

4.4 Redshift evolution of kinematic and photometric properties

In this subsection we look at the evolution of three global parameters, λ_R, ξ_3, and a_4/a, through the whole formation history of our case-study simulation. We first use λ_R (equation 8) to quantify the redshift evolution of specific angular momentum in the *AGN* and *NoAGN* cases. Fig. 7 shows the redshift evolution of λ_R from $z = 2$ to $z = 0$. After a tumultuous phase at high redshift caused by mergers, at $z = 1$ λ_R settles at around 0.3–0.4 in both cases.

Downloaded from https://academic.oup.com/mnras/article-abstract/489/2/2702/5556548 by Said Business School user on 05 November 2019

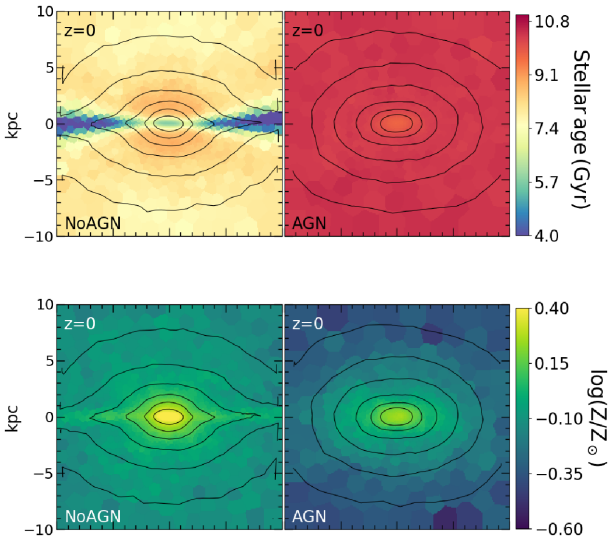

Figure 6. Voronoi binned maps of the (mass-weighted) average stellar age (top) and metallicity (bottom) for our case-study galaxy (0227), in the *NoAGN* (left-hand panel) and *AGN* (right-hand panel) AGN cases, at $z = 0$. Without AGN feedback the higher star-formation rate at low redshift produces an overall much younger system, especially in the mid-plane, where a young stellar disc forms. Higher star-formation rate also results in high metallicities. With AGN feedback (right-hand panels) the galaxy is instead very old and its average metallicity is lower, closer to what we expect from observed early-type galaxies with this stellar mass (see e.g. McDermid et al. 2015 for a statistical study, or Guérou et al. 2016 for an example of spatially resolved age/metallicity maps).

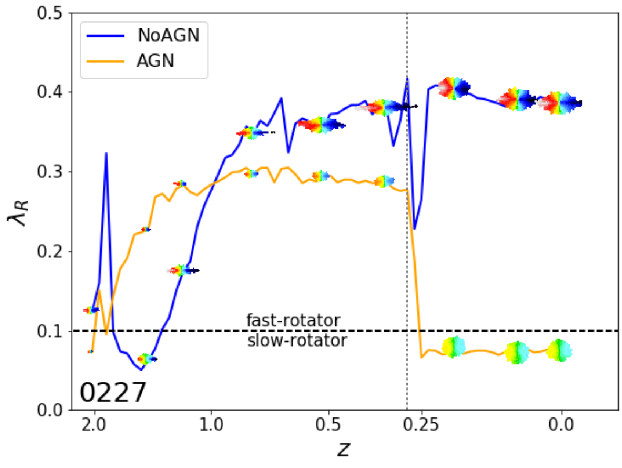

Figure 7. Evolution of λ_R for galaxy 0227, in the *NoAGN* and *AGN* cases. The values are indicated by inserted velocity maps out to the effective radius (isophote) of the galaxies. A major merger at $z \sim 0.25$ (vertical dotted line) strongly reduces the angular momentum of both systems. The *NoAGN* galaxy is less affected and can quickly regain angular momentum due to gas accretion and star formation. The *AGN* galaxy is instead unable to form new stars and remains a slow rotator.

At $z = 0.25$ the angular momentum drops because of the major merger described in Section 4.1; the vertical dotted line marks the beginning of this merger. The subsequent evolution diverges for the two cases. In the *NoAGN* simulation the system is more gas rich, and thus loses less angular momentum and even regains it after the merger. This is a typical feature of gas-rich mergers and follow-up gas accretion (see review by Naab & Ostriker 2017). In

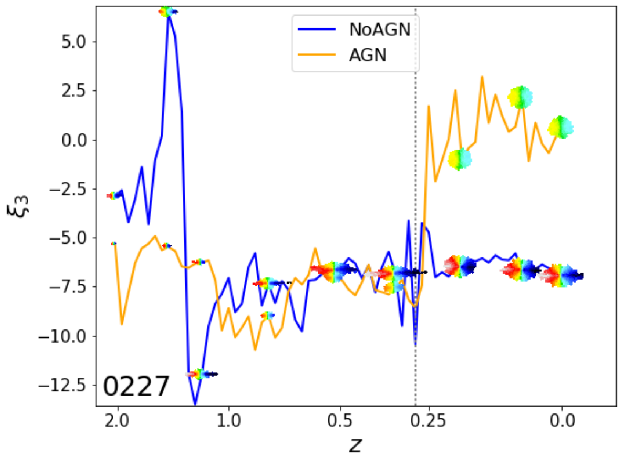

Figure 8. Evolution of ξ_3 for galaxy 0227, in the *NoAGN* and *AGN* cases. The values are indicated by small velocity maps out to the effective radius (isophote) of the galaxies. Up to $z = 0.25$ the value of ξ_3 is constant for both simulations and has a value as expected for a rotating system. However, after a major merger at $z \sim 0.25$ (vertical dotted line), the value for the *AGN* galaxy shifts towards zero and mildly positive values. This indicates that the galaxy lost its rotational support.

the *AGN* case the system is already gas poor, without significant star formation before the merger (see Fig. 3). The merger then reduces the angular momentum significantly. Qualitatively this process for gas-poor mergers is discussed in detail in Naab et al. (2014). By $z = 0$ the two systems have very different rotation properties with a λ_R value typical of fast rotators in the *NoAGN* case and a slow rotator value in the *AGN* case. This impact of AGN feedback on the rotation properties of massive galaxies has already been reported by Dubois et al. (2013), Martizzi et al. (2014), and Dubois et al. (2016) for cosmological RAMSES adaptive mesh refinement simulations with different AGN feedback models. We therefore assume this to be a generic feature of AGN feedback.

The major merger also affects the higher order kinematic features. We quantify them using the parameter ξ_3 defined in equation (9) and plot it as a function of redshift, as shown in Fig. 8. From $z = 1$ to $z = 0.25$ the two simulations show again the same behaviour, with the same degree of anticorrelation between h_3 and $V_{\rm avg}$ / σ: $\xi_3 \sim -7.5$ in both cases. As discussed in Section 3.2, this value is typical for a system dominated by tangential orbits, but higher than the one expected from a purely rotational system (-10). This indicates that a small amount of other orbit types contributes to skew the LOS velocity distribution. The major merger at $z = 0.25$ again makes the two cases diverge. In the *NoAGN* case the overall ξ_3 value stays the same. In the *AGN* case instead ξ_3 drops to 0 and the orbital structure of the system is more dispersion-supported – the correlation between h_3 and $V_{\rm avg}/\sigma$ becomes weaker. The sign of ξ_3 oscillates a bit, but then settles to a weakly positive value, meaning that h_3 has the same sign as $V_{\rm avg}$ as already pointed out.

We investigate the evolution of the isophotal shape parameter a_4/a, obtained by fitting the galactic isophotes at every snapshot (see subSection 3.3), with the galaxy seen edge-on. An example of these isophotes can be seen in the black lines of Figs 4 and 5. We show the evolution of a_4/a since $z = 2$ in Fig. 9. Unlike in the previous cases, the *AGN* and *NoAGN* cases are already different at $z = 1$. The *NoAGN* case has systematically higher values of a_4/a – more discy isophotes. This difference would however not be as

Downloaded from https://academic.oup.com/mnras/article-abstract/489/2/2702/5556548 by Said Business School user on 05 November 2019

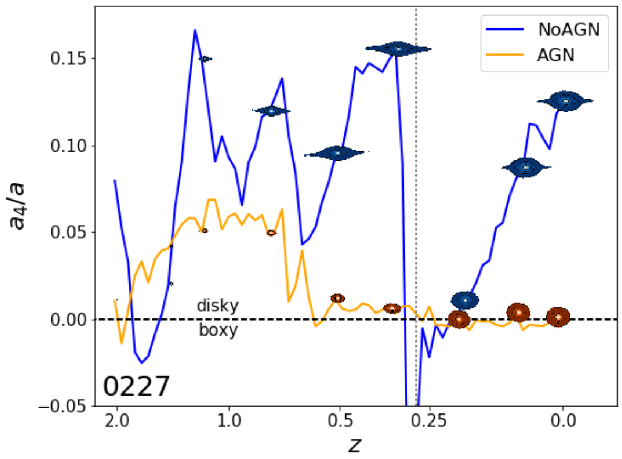

Figure 9. Evolution of the isophotal shape of galaxy 0227, in the *AGN* and *NoAGN* case, quantified by a_4/a. The markers are surface brightness maps cut along the effective isophote. The red line represents perfectly elliptical isophotes. 'Boxy' galaxies have negative, 'discy' galaxies have positive a_4/a values. Without AGN feedback the formation of a prominent disc results in discy isophotes at all times, despite the major merger at $z \sim 0.25$ (vertical dotted line). The *AGN* galaxy instead loses its discyness after the merger because further star formation is suppressed by the AGN.

pronounced if the galaxy was not seen from an edge-on perspective. The value scatters due to minor mergers but drops to negative values after the major merger at $z = 0.25$. This is the common feature of major mergers destroying previously existing disc structures (see Naab et al. 1999; Naab & Burkert 2003). Subsequently a new stellar disc forms and the a_4/a value becomes strongly positive again. In the *AGN* case the galaxy already lost its discyness at high redshift, because of the suppressed inflow of high-angular-momentum star-forming gas, and it keeps its elliptical or mildly boxy isophotes to $z = 0$. The effect of mergers and AGN feedback on the isophotal shape points in the same direction as the effect on λ_R and ξ_3.

4.5 Kinematics of the accreted and *in-situ*-formed stellar components

Our kinematic maps can be generated for different stellar components of the galaxy to shed light on their respective kinematic structure. One might use the stellar age to distinguish different components; we show this example in the appendix. Perhaps even more interesting though, is to separate stellar particles according to their origin: either accreted from another galaxy or formed *in situ* in the main progenitor following the accretion of gas. Due to their intrinsically different origin, we can expect these two components to show very different kinematic (and stellar population) signatures (see e.g. Naab et al. 2014). To classify stars as *in situ* or accreted, we trace stars in the galaxies throughout the simulation from $z = 2$ to $z = 0$, and label them as *in-situ* stars when they form within 10 per cent of the virial radius (see Oser et al. 2010). All the remaining stellar particles are labelled as accreted. In the case of galaxy 0227 the *in-situ* fraction is $f_{\text{in-situ}} = 0.50$ and $f_{\text{in-situ}} = 0.17$ for the *NoAGN* and *AGN* cases, respectively. The values for the other galaxies are shown in Table 1.

Figs 10 and 11 show the stellar kinematic maps obtained for the separated *in-situ* and accreted components, in the *NoAGN* and *AGN* cases, respectively. The accreted components (upper panels of Figs 10 and 11) exhibit a very high velocity dispersion in both cases, but also have considerable net rotation, especially in the *NoAGN* case. This larger net rotation is probably caused by the potential being more oblate-shaped in the *NoAGN* simulation ($T = 0.41$). In the *AGN* case the galaxy has a very triaxial, almost prolate shape ($T = 0.86$), which hinders the amount of z-tube orbits (more on this in Section 4.6) causing less rotation. The different shape is likely caused by the $z = 0.25$ merger being more gas-poor in the *AGN* case.

The *in-situ* components are very different in the two cases. In the *AGN* case (lower panel of Fig. 11), the *in-situ* stars follow the same kinematics as the accreted ones. Almost all of these stars formed before the major merger at $z = 0.25$, which means that their original orbits have been scrambled, resulting in a dispersion-supported system. In the *NoAGN* case the number of *in-situ*-formed stars is larger, both before and after the major merger, and the corresponding kinematic maps are more complex. There are two distinct features. The first is an orderly fast-rotating disc in the mid-plane, with low-velocity dispersion, a shallow h_3-V_{avg}/σ trend, and strongly negative h_4. The second is a slow-rotating bulge with high velocity dispersion and a much steeper trend with h_3. The first component is mostly made of young stars which formed after the $z = 0.25$ major merger, hence the orderly motion. The surrounding bulge is instead older. These stars formed *in situ* at $z > 0.25$, and their orbits have been scrambled because of the major merger, resulting in less rotation. As the very high velocity dispersion suggests, there is also a counter-rotating component in this bulge, which explains why this component has a smaller net rotation than the accreted stars in the same potential.

This analysis implies that *in-situ*-formed stars and accreted stars tend to have intrinsically different kinematics from one another, at least until a major merger event scrambles their orbits. AGN feedback can thus significantly alter the present-day kinematics of galaxies by limiting *in-situ* star formation at late times, 'freezing' the kinematics at the most recent major merger, but also by affecting the merger history of the galaxy and thus the accreted stellar component.

4.6 Orbit distribution

It is also of interest to directly study the distribution of stellar orbits, and how it is affected by AGN feedback. We classify star particles into four global orbit types: z-tubes (rotating around the z-axis), x-tubes (rotating around the x-axis, including inner and outer major axis tubes), boxes (including π-boxes and boxlets), and irregular orbits. Fig. 12 shows the fraction of these orbit families as a function of radius. In both the *AGN* and *NoAGN* cases box orbits dominate within the central region, while tube orbits become dominant in the outer parts. In the *NoAGN* case, the fraction of z-tube orbits is larger at almost all radii. This is expected given the very prominent disc that has formed at low redshift. In the *AGN* case the z-tube fraction drops from 65 per cent to 49 per cent. The fraction of box orbits is lower in the centre and higher in the outskirts. The biggest change is however in the fraction of x-tube orbits, which went from an overall 5 per cent to 17 per cent. The likely reason for this is that the potential of the *AGN* galaxy has a more prolate shape ($T = 0.86$, instead of $T = 0.41$ for the *NoAGN* case), allowing for this kind of orbits. This change in the relative fraction of different orbit families also explains the positive correlation between h_3 and V_{avg}/σ; the bulk of the LOS velocity distribution is made of x-tube, box, and retrograde z-tube orbits, and the prograde z-tube orbits add a high-velocity tail to it. The fraction of irregular orbits is very low (< 5 per cent) in both cases. For about 20 per cent of the stellar particles our orbit classification scheme failed (see Section 3.4), and they are not included in the figure.

Downloaded from https://academic.oup.com/mnras/article-abstract/489/2/2702/5556548 by Said Business School user on 05 November 2019

Table 1. General properties of our sample of simulated galaxies.

GalID		$M_\star(10^{10}\,M_\odot)$	R_e	Avg. age (Gyr)	$f_{\text{in-situ}}$	ϵ	a_4/a	T	λ_R	ξ_3	$f^{\text{pro}}_{\text{z-tube}}$
0175	NoAGN	26.73	1.86	7.85	0.23	0.24	0.017	0.72	0.08	−0.05	0.22
0175	AGN	18.93	2.57	10.72	0.05	0.35	0.001	0.51	0.12	−6.58	0.34
0204	NoAGN	19.59	3.09	8.17	0.63	0.78	0.196	0.29	0.46	−7.07	0.66
0204	AGN	16.41	2.06	9.50	0.18	0.37	0.026	0.15	0.36	−8.19	0.60
0215	NoAGN	27.79	1.76	9.61	0.27	0.38	0.042	0.48	0.37	−5.14	0.53
0215	AGN	7.38	1.70	11.26	0.09	0.31	0.018	0.50	0.02	−0.79	0.13
0227	NoAGN	48.46	3.27	7.72	0.50	0.49	0.124	0.41	0.47	−8.10	0.68
0227	AGN	22.24	2.60	9.95	0.15	0.15	0.000	0.86	0.10	0.50	0.20
0290	NoAGN	26.32	2.95	8.55	0.57	0.71	0.112	0.28	0.52	−11.49	0.74
0290	AGN	12.67	2.57	10.45	0.25	0.38	0.045	0.66	0.06	−2.62	0.23
0408	NoAGN	10.82	1.84	8.44	0.53	0.24	0.020	0.37	0.45	−5.96	0.53
0408	AGN	11.11	1.68	9.06	0.44	0.43	0.055	0.13	0.28	−6.48	0.50
0501	NoAGN	6.80	1.74	10.71	0.10	0.33	0.029	0.22	0.42	−6.74	0.54
0501	AGN	8.25	1.93	11.22	0.10	0.30	0.018	0.44	0.10	−3.55	0.26
0616	NoAGN	8.61	1.29	8.87	0.31	0.38	0.055	0.09	0.04	−1.02	0.13
0616	AGN	4.56	1.53	11.07	0.06	0.35	0.010	0.36	0.35	−7.27	0.50
0664	NoAGN	8.04	1.15	9.50	0.36	0.41	0.031	0.37	0.44	−5.74	0.24
0664	AGN	7.23	1.38	10.51	0.20	0.43	0.052	0.09	0.32	−7.61	0.67
0858	NoAGN	9.95	1.54	6.65	0.68	0.36	0.045	0.40	0.41	−8.85	0.58
0858	AGN	8.43	1.58	8.15	0.59	0.26	0.006	0.83	0.25	−6.88	0.19

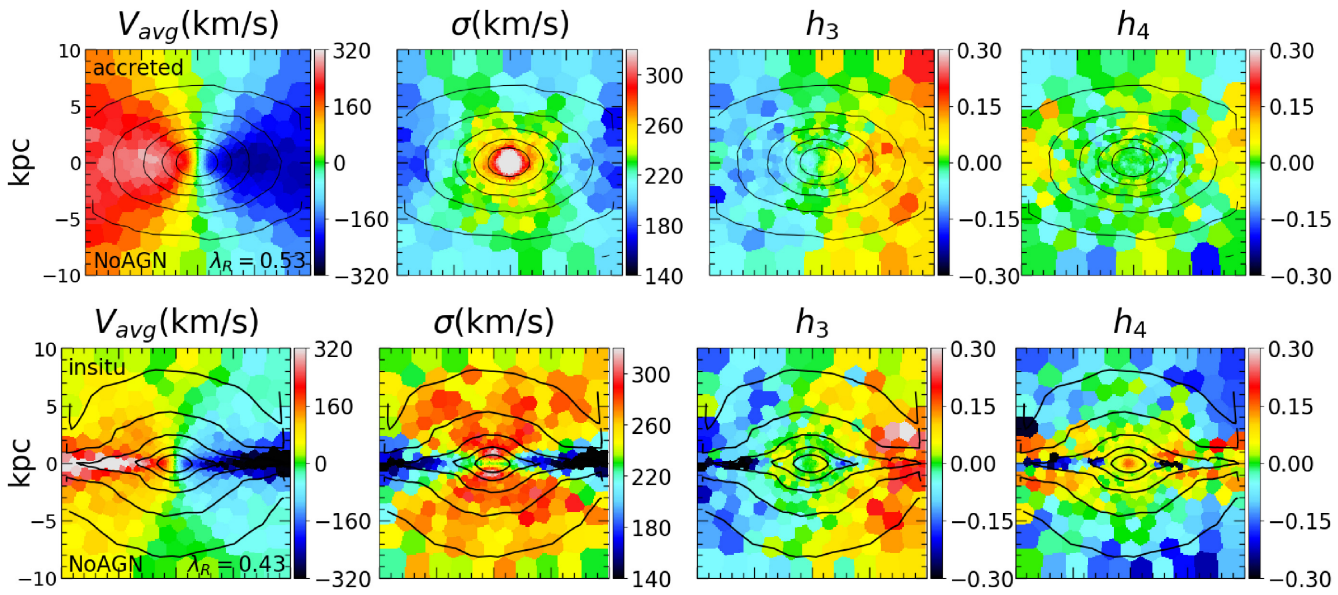

Figure 10. Stellar kinematics of galaxy 0227 (NoAGN) separated into its accreted component (above) and its *in-situ* formed one (below). The overall *in-situ* fraction is 50 per cent. The two components have strikingly different kinematics. The accreted component is mainly pressure-supported, but also rotates fast. The *in-situ* component shows two distinct features: a fast-rotating disc in the mid-plane with low velocity dispersion, and a slow-rotating bulge with very high velocity dispersion. The disc feature formed after a recent major merger, while the surrounding bulge is older, and its originally rotational orbits have been scrambled by the merger.

The effect of AGN feedback on stellar orbits was also investigated in Bryan et al. (2012), who found a sharp increase in the fraction of box orbits. We do not see this in galaxy 0227, where the suppression of z-tube orbits is balanced by the increase in x-tube orbits. We however do see a trend towards more box orbits in the other galaxies of our sample, which will be discussed (and compared to Bryan et al. 2012) in Section 5.3.

5 RESULTS FROM THE SIMULATION SAMPLE

So far we focused on a single, example galaxy. In this section we show more general results for all 20 galaxies in our sample. This analysis cannot reveal the statistical kinematic properties of quiescent galaxy populations from recent cosmological simulations (Dubois et al. 2016; Penoyre et al. 2017b; Lagos et al. 2018; Schulze

Downloaded from https://academic.oup.com/mnras/article-abstract/489/2/2702/5556548 by Said Business School user on 05 November 2019

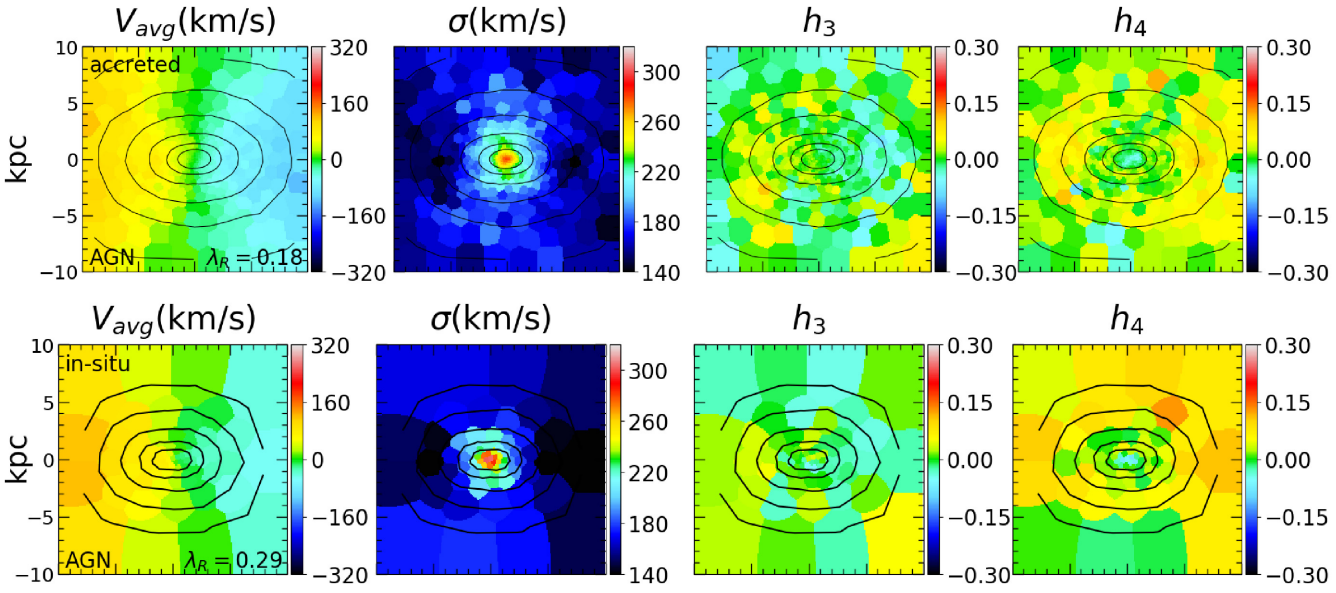

Figure 11. Stellar kinematics of the accreted (above) and *in-situ* formed (below) stars of galaxy 0227 simulated with AGN feedback. The overall *in-situ* fraction is 17 per cent . In both cases the kinematics are pressure-supported, as no star formation happened since the last major merger at $z = 0.25$.

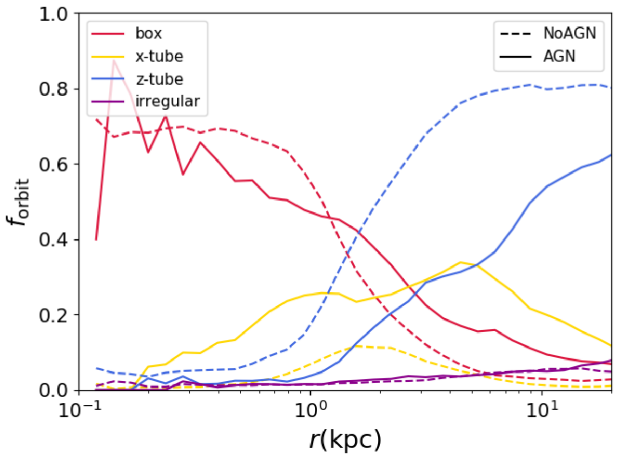

Figure 12. Radial frequency of three different types of orbits in our case study galaxy: z-tubes, x-tubes, boxes, and irregular orbits. The dashed line shows the *NoAGN* case, and the full line shows the *AGN* one. In the latter, the fraction of z-tube orbits drops considerably due to the suppression of disc formation, and the fraction of x-tube orbits increases due to the more triaxial potential.

et al. 2018). Instead, we would like to highlight the detailed impact of AGN feedback on massive galaxies for a few individual systems simulated at higher resolution. Table 1 shows for each galaxy in our sample the stellar mass $M_\star$, effective radius R_e, the average stellar age, the *in-situ* formed fraction, the ellipticity ϵ, the isophotal shape a_4/a, the triaxiality parameter T, λ_R, ξ_3, and the fraction of z-tube orbits $f_{\text{z-tube}}$. The galaxy IDs refer to a $z = 0$ halo in the parent simulation (the same as in Oser et al. 2012; Naab et al. 2014,...) and are ordered by halo mass. In general our galaxies have a lower stellar mass with AGN feedback due to the quenching of star formation, while the effective radius (for a given stellar mass) increases due to less dissipation (e.g. Crain et al. 2015; Choi et al. 2018). There are however notable exceptions: galaxies 0408 and 0501 have a larger stellar mass with AGN feedback. In both these cases the *NoAGN* simulations go through strong stellar feedback events after high redshift starbursts, which result in a lot of gas leaving the galaxy. In the *AGN* case this does not happen, possibly because star formation happens more gradually. This causes the gas to stay in the galaxy and over time form more stars. Despite this, both systems experience less late star formation with AGN feedback, and at $z = 0$ have older ages and lower λ_R values. In the following sections we will look at the distribution of kinematic (λ_R, ξ_3, orbit families) and morphological (a_4/a, triaxiality) properties at $z = 1$ and $z = 0$, and how AGN feedback affects them.

5.1 Angular momentum

In Fig. 13 we plot the λ_R parameter of the sample galaxies versus their ellipticity ϵ for the simulations without (*NoAGN*, left-hand panels) and with AGN (*AGN*, right-hand panels) at redshift $z = 1$ (top panels) and $z = 0$ (bottom panels). The location of edge-on projections are indicated by the velocity maps. The blue/orange shaded regions indicate the typical distribution of these systems for 50 random orientations (projection effects for λ_R based on simulations are discussed in e.g. Jesseit et al. 2009; Naab et al. 2014; Lagos et al. 2018). They were obtained by rotating the galaxies according to random rotation matrices, which were generated with the Stewart (1980) algorithm. The red line separates slow and fast rotators following to the definition by Cappellari (2016). A galaxy is considered a slow-rotator when

$$\lambda_R < 0.08 + 0.25\,\epsilon \qquad \text{with} \qquad \epsilon < 0.4. \tag{17}$$

The distribution of galaxies at $z = 1$ is similar between the *AGN* and *NoAGN* cases, with most galaxies being flattened fast rotators with λ_R in the range $0.2 < \lambda_R < 0.4$. The ellipticity values are a bit higher in the *NoAGN* case ($0.3 < \epsilon < 0.8$) than in the *AGN* one ($0.3 < \epsilon < 0.6$), but qualitatively the two populations are very similar. By $z = 0$ many (7 out of 10) of the *NoAGN* galaxies are still fast rotators with a similar ellipticity distribution. This trend is in agreement with results for massive galaxy populations from cosmological box simulations without AGN feedback (Dubois et al.

Downloaded from https://academic.oup.com/mnras/article-abstract/489/2/2702/5556548 by Said Business School user on 05 November 2019

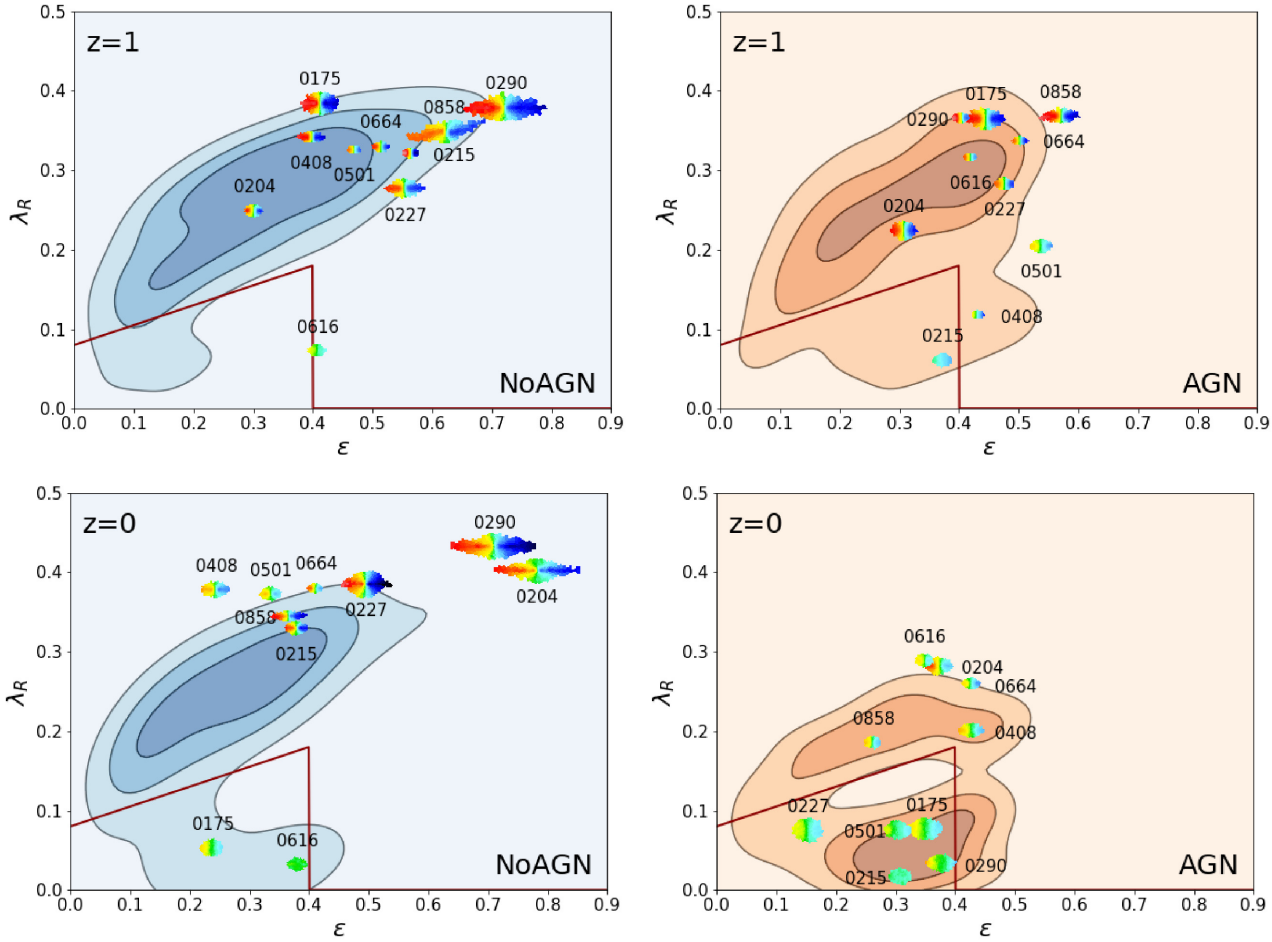

Figure 13. λ_R as a function of ellipticity ϵ for the galaxies at redshift $z = 1$ (top panels) and $z = 0$ (bottom panels), simulated without (*NoAGN*, left-hand panel) and with (*AGN*, right-hand panel) AGN feedback. The edge-on values are indicated by velocity maps. The coloured contours indicate the distribution of our galaxies when they are seen from 50 random orientations each. The dark red line marks the limit between slow- and fast-rotators according to Cappellari (2016). With AGN feedback the systems become rounder and rotate more slowly at z = 0.

2016). Instead, in the *AGN* case by $z = 0$ the galaxies have become rounder ($\epsilon < 0.4$) and more slowly rotating, with λ_R no larger than ∼0.35. More than half of the galaxies would be considered bona fide slow rotators even in their edge-on projections. As discussed earlier, the trend towards slower rotation with AGN feedback is caused by the suppression of late *in-situ* star formation (see Brennan et al. 2018 for a discussion of ejective and preventative AGN feedback), which in most cases significantly reduces rotation observed at $z = 0$. The effect is strongest for the largest and most massive galaxies in our samples (lower numbers, like 0227), which – without AGN feedback – develop massive fast-rotating disc structures (in the case of galaxy 0175, this young disc structure is on a different plane, and thus does not increase λ_R significantly).

We find a correlation between λ_R and ϵ, at least for the fast-rotators: faster rotating galaxies tend to be more flattened. Most of our slow-rotating galaxies exhibit a relatively high ellipticity, which is a trend found in other simulation studies as well (Bois et al. 2010; Naab et al. 2014), and possibly due to resolution limits. An interesting case is galaxy 0616, which contradicts our expectations by being a slow-rotator when simulated without AGN feedback but turns into a fast-rotator when simulated with AGN feedback. What happens here? In the *NoAGN* case gas infall triggers a starburst that forms a disc that counter-rotates with respect to the rest of the galaxy. This lowers the projected λ_R value, but leaves a relatively high ellipticity. In the *AGN* case the gas is kept from forming this new disc and the galaxy retains most of the (projected) angular momentum of the older stellar component.

In Fig. 14 we plot the λ_R radial profiles for all galaxies, at $z = 1$ and $z = 0$. Typically, the values increase from the centre until they reach an asymptotic value, usually within R_e. This is consistent with previously published simulation data, even though we are missing systems with dropping λ_R profiles (Naab et al. 2014; Wu et al. 2014; Lagos et al. 2018). At $z = 1$ there is not much difference between the *AGN* and *NoAGN* galaxies, while at $z = 0$ galaxies simulated with AGN feedback show once again systematically lower λ_R values, even among the fast rotators. Many galaxies that would be rotationally supported without AGN, become pressure-supported when an AGN is present. Overall, AGN feedback results in more slow-rotating and dispersion-supported galaxies in agreement with previous simulations (Dubois et al. 2016).

5.2 Higher order kinematics

As discussed in Sections 3.2 and 4.4, rotating galaxies are expected to have anticorrelated h_3 and velocity fields, but the degree of this anticorrelation depends on the orbital structure of the galaxy, and

Downloaded from https://academic.oup.com/mnras/article-abstract/489/2/2702/5556548 by Said Business School user on 05 November 2019

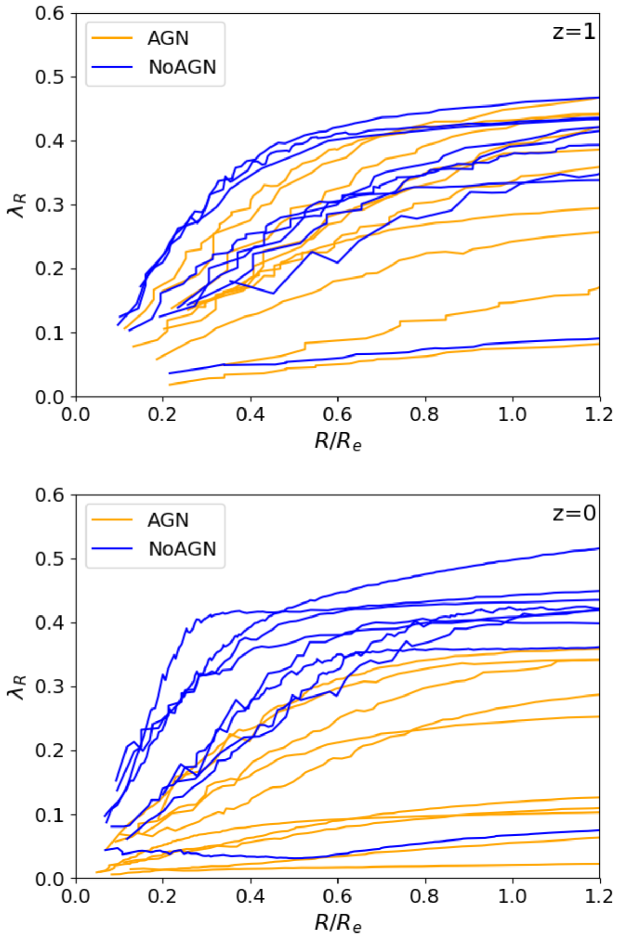

Figure 14. λ_R radial profiles of our galaxy sample at z = 1 (top) and z = 0 (bottom). The *AGN* galaxies (orange) evolve towards lower λ_R values than their *NoAGN* counterparts (blue).

we can employ our ξ_3 parameter to evaluate this for our sample. In Fig. 15 we plot ξ_3 as a function of λ_R at $z = 1$ and $z = 0$. The edge-on values are plotted with velocity maps, while the contours represent the location of the sample in the ξ_3– λ_R plane for random orientations. At $z = 1$ all galaxies have a negative of ξ_3 and h_3 is anticorrelated with the velocity, as expected for fast rotators. This is also true for the two galaxies which are slow rotators (according to λ_R) at $z = 1$. At $z = 0$ the sample splits into two groups: slow rotators with low values of λ_R tend to have $\xi_3 \sim 0$ (very steep correlation or no correlation), while all fast rotators have $\xi_3 < -3$ (negative correlation). The specific value of ξ_3 for the fast rotators depend on their orbital structure; the galaxies where a disc feature is particularly prominent (0204, 0227, and 0290 in the *NoAGN* case) have the lowest values, reaching about $\xi_3 = -11.5$. In other words, more flattened and simple rotating systems have a less steep correlation between h_3 and $V_{\rm avg}/\sigma$ than fast rotators with more complex kinematics. A similar behaviour was also observed in real galaxies by Veale et al. (2017). This results in a weak correlation between ξ_3 and λ_R for the fast rotators that was not present at $z = 1$ when the kinematics of the galaxies were overall simpler. The bimodality of slow and fast rotators in the $\xi_3 - \lambda_R$ plane is seen in both the *NoAGN* and *AGN* cases, but with AGN feedback the group of galaxies with $\xi_3 \sim 0$ is larger. A few galaxies (0175 *NoAGN*and 0227 *AGN*) have a positive value of ξ_3 at $z = 0$ when viewed from certain orientations.

If we compare these results with observational IFU surveys, we find a small discrepancy. In Fig. 16 we plot the ξ_3 values of galaxies from the ATLAS^{3D} survey (Cappellari et al. 2011b),[2] compared with the contours of our *AGN* simulations seen at random inclinations. The ATLAS^{3D} values also include a re-extraction of the kinematics from the subset of galaxies in the SAURON survey originally presented in Emsellem et al. (2004). To compute ξ_3 and λ_R for the ATLAS^{3D} sample, we only considered spaxels with $\sigma > 120\,{\rm km\,s^{-1}}$, since the Gauss–Hermite moments can only be extracted from the data when the galaxy velocity dispersion is well resolved by the spectrograph (e.g. Cappellari & Emsellem 2004). The distribution of ξ_3 values is similar between observations and simulations, and can be divided in two groups: slow rotators with $\xi_3 \sim 0$ and fast rotators with $-3 < \xi_3 < -10$. However, at given λ_R the ATLAS^{3D} galaxies seem to have lower ξ_3 (in absolute value) than the simulations. We believe there are at least three reasons for this difference. Several of the ATLAS^{3D} fast rotators have strong bar features, which are not present in our sample of simulations. In their presence the kinematic maps often show a positive correlation between $V_{\rm avg}$ and h_3 (Chung & Bureau 2004), causing ξ_3 values closer to zero or sometimes even positive. In Fig. 16 galaxies with clear bars have been highlighted, and they tend to have slightly larger ξ_3, although this does not seem to account for all ATLAS^{3D} fast rotators with ξ_3 close to zero. It is possible that hidden or weak bars are present in the other galaxies too, affecting the h_3 values. Secondly, as previously mentioned, constraining the h_3 value of each spaxel is harder in observations. The selection of spaxels with $\sigma > 120\,{\rm km\,s^{-1}}$ limits this problem, but does not eliminate it. This results in more noisy h_3 maps, which makes the h_3–$V_{\rm avg}/\sigma$ trend less tight, and thus moves the ξ_3 value of observed galaxies closer to zero. At equal σ, this effect is stronger for slower rotating galaxies, as their LOS velocity distribution have lower h_3 values. Lastly, our (*AGN*) sample consists of only 10 massive galaxies, all of which have relatively low λ_R values. This could be coincidental, but could also be caused by the limitations of AGN feedback models, which are known to be difficult to control and in this case might struggle to produce true fast rotators. If our *AGN* simulations did explore the $\lambda_R > 0.3$ regime, we would however expect most of them to have $-10 < \xi_3 < -5$, typical of rotation-dominated systems, matching the observations.

5.3 Orbit distribution and connection to kinematic correlation

The fraction of prograde z-tube orbits $f^{\rm pro}_{\rm z\text{-}tube}$ of the galaxies in our sample, measured in the same way as in Sections 3.4 and 4.6, are listed in Table 1. We generally find slightly lower prograde z-tube fractions in the *AGN* sample compared to the *NoAGN* one. A trend in this direction was also found by Bryan et al. (2012), who similarly derived the fractions of different orbit types in cosmological simulations with and without AGN feedback, although they focused on larger haloes and at large radii. If we compare our simulations at the same radius, we however find a weaker dependence on AGN feedback. In Bryan et al. (2012) the median fraction of tube orbits within 0.1 $R_{\rm vir}$ goes from 45 per cent without AGN feedback (in their fiducial REF simulation) to 20 per cent with AGN. In our sample it goes from 63 per cent to 48 per cent. Similarly, the box orbit fraction of Bryan et al. (2012) goes from 50 per cent to almost 80 per cent, while in our simulations it stays much lower, from 20 per cent without AGN to 25 per cent with. This difference is likely due to

[2] Available from http://purl.org/atlas3d

Downloaded from https://academic.oup.com/mnras/article-abstract/489/2/2702/5556548 by Said Business School user on 05 November 2019

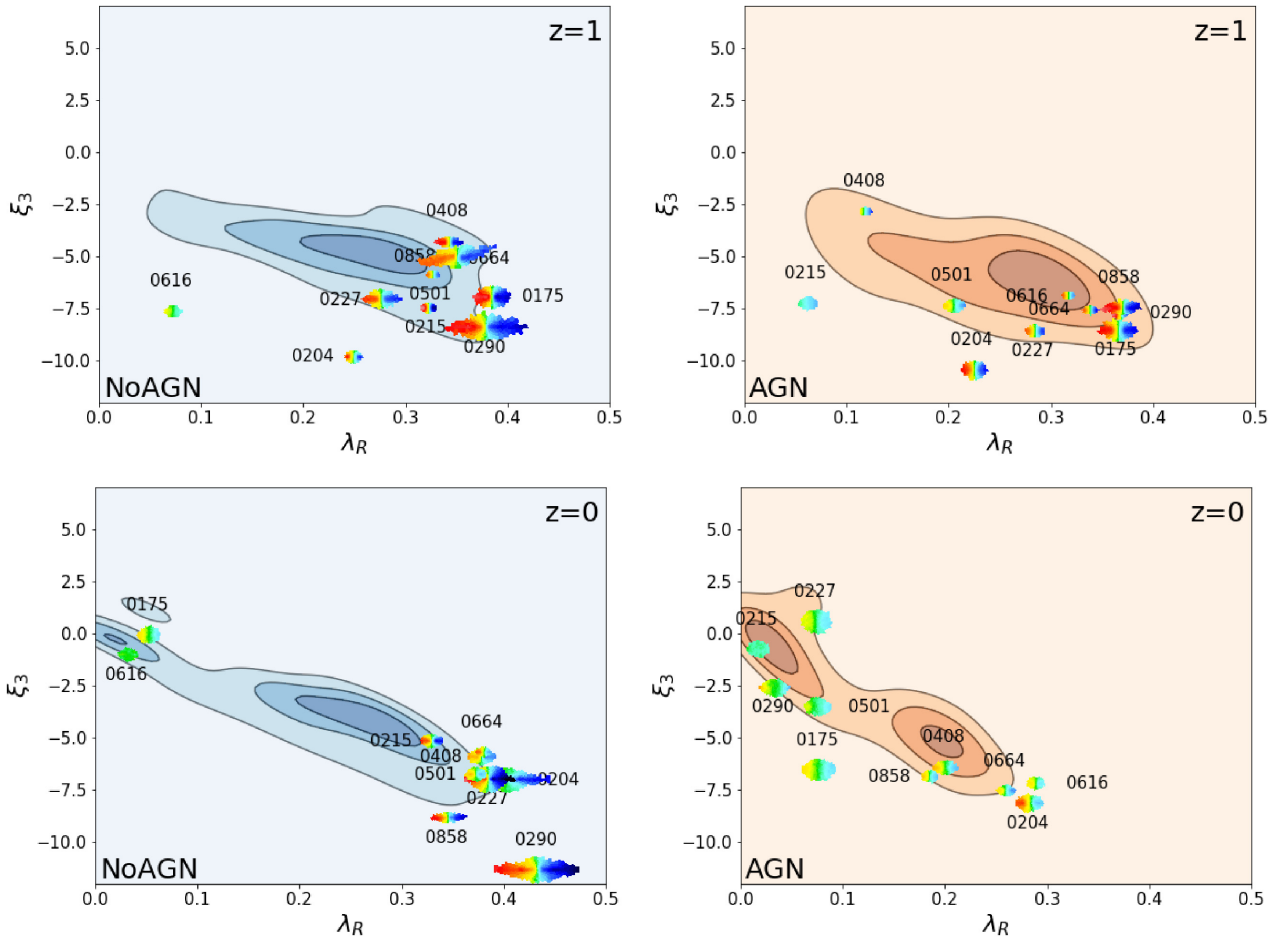

Figure 15. ξ_3 versus λ_R at $z = 1$ (top panels) and $z = 0$ (bottom panels), simulated without (left-hand panel) and with (right-hand panel) AGN feedback. The kinematic map markers indicate the values when the galaxy is seen edge-on, while the density contours indicate the distribution when our galaxies are seen through 50 random orientations each. At $z = 1$ all galaxies have values of ξ_3 in the anticorrelation regime, typical of fast rotators, while at $z = 0$ many galaxies have $\xi_3 \sim 0$ or in a few cases even positive, and this effect is stronger with AGN feedback.

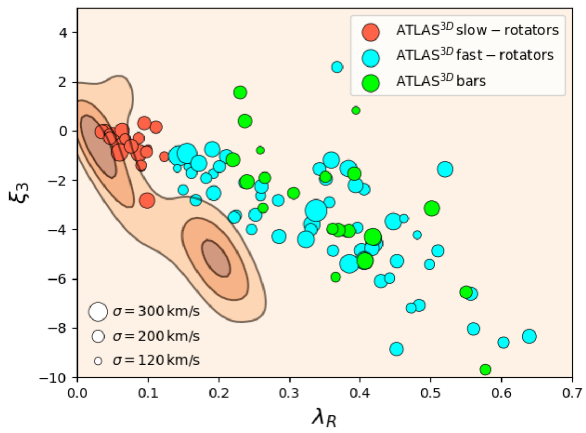

Figure 16. ξ_3 as a function of λ_R for the galaxies from the ATLAS^{3D} sample (circle markers), compared with our *AGN* simulations (orange contours; same as Fig. 15). The ATLAS^{3D} galaxies are distinguished in slow-rotators (red) and fast-rotators (light blue) according to the Cappellari (2016) definition. At equal λ_R, observed fast-rotators seem to have smaller ξ_3 (absolute) values than the simulation, possibly because of more complex kinematic features (bars) and of more noisy h_3 measurements. Slow-rotators have $\lambda_R \sim 0$ and $\xi_3 \sim 0$ in both observations and simulations.

their more massive halo sample; their mean dark matter halo mass is $6\,10^{13}\,h^{-1}\,\mathrm{M}_\odot$, meaning that they contain galaxy groups rather than single galaxies. This explains the larger box orbit fractions, as *in-situ* star formation, which favours tube orbits, is less important at this scale. It also explains why in the Bryan et al. (2012) sample stars and dark matter particles roughly have the same orbital structure, which would not be true in our sample. The difference could however also be due to the different simulation code used in this work, particularly the stellar and AGN feedback models.

The kinematic correlation parameter ξ_3 that we introduced is related to the orbital structure of galaxies. Here we would like to study this connection using our orbit analysis. In Fig. 17 we plot ξ_3 as a function of the fraction of prograde z-tube orbits within R_e, $f^{\mathrm{pro}}_{\mathrm{z\text{-}tube}}$, at $z = 0$. The plotted ξ_3 values are the average for 50 random views of each galaxy, and the error bars mark the dispersion (negligible for galaxies 0616 *NoAGN* and 0215 *AGN*, because they have projected velocity maps close to zero; see the kinematic map markers in Fig. 15). Most galaxies with high values of $f^{\mathrm{pro}}_{\mathrm{z\text{-}tube}}$ have a $\xi_3 < -3$ as expected, and there is a rough correlation between the two quantities. The galaxy with the highest $f^{\mathrm{pro}}_{\mathrm{z\text{-}tube}}$ (0290 *NoAGN*) is also the one with the lowest value of ξ_3: ~ -11.5 when seen edge-on and ~ -6.5 when averaging between many different viewing angles. The reason for this is that when the system is dominated by orbits

Downloaded from https://academic.oup.com/mnras/article-abstract/489/2/2702/5556548 by Said Business School user on 05 November 2019

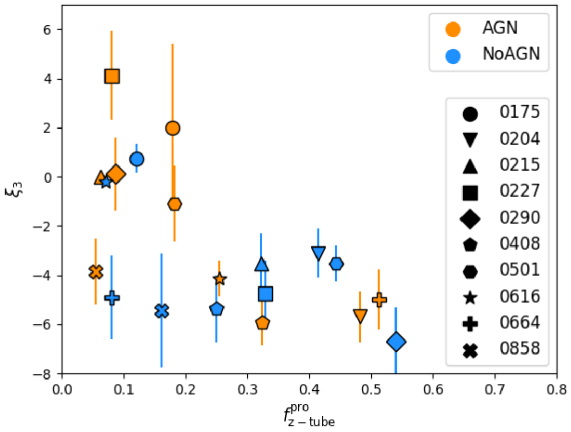

Figure 17. ξ_3 as a function of the fraction of prograde z-tube orbits $f^{\rm pro}_{\rm z\text{-}tube}$ for our sample of simulated galaxies at $z = 0$. The ξ_3 values of each galaxy are an average over 50 random views, and the error bars are their standard deviation. Galaxies with high $f^{\rm pro}_{\rm z\text{-}tube}$ tend to have $\xi_3 < -5$.

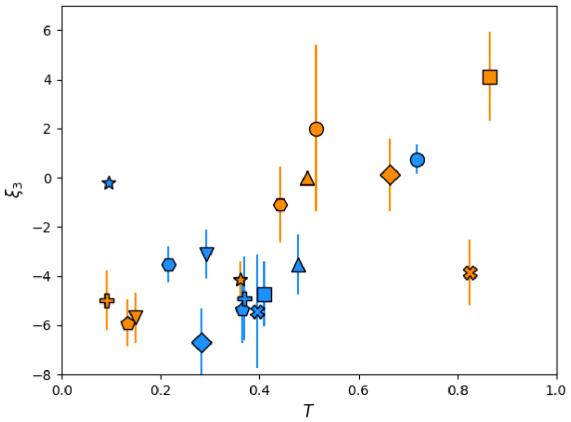

Figure 18. ξ_3 as a function of the triaxiality parameter for our sample of simulated galaxies at $z = 0$. The ξ_3 values of each galaxy are an average over 50 random views, and the error bars are their standard deviation. There is a correlation between the two parameters: prolate galaxies have positive values of ξ_3 , while oblate galaxies have negative values.

that rotate (progradely) around the z axis, these stars form the bulk of the LOS velocity distribution, and all other orbit types make the h_3 signal stronger for that given $V_{\rm avg}/\sigma$. When non-rotational orbits are dominating ($f^{\rm pro}_{\rm z\text{-}tube} \sim 0$), then $V_{\rm avg}/\sigma \sim 0$ and consequently $\xi_3 \sim 0$.

A few galaxies (0175 *NoAGN* and 0227 *AGN*) have a positive correlation between h_3 and $V_{\rm avg}/\sigma$ in large parts of their kinematic maps, resulting in a positive value of ξ_3. This is likely connected to the fact that these galaxies have a prolate potential. We investigate this by plotting ξ_3 as a function of the triaxiality parameter T in Fig. 18. There seems to be a rough correlation between the two quantities in our sample. The most prolate galaxies ($T \sim 1$) have positive values of ξ_3, while almost all oblate galaxies ($T < <1$) have negative values. An exception is galaxy 0616 *NoAGN*, which as already discussed is made of two counter-rotating components and looks like a 'fake' slow rotator.

This connection between morphology and kinematics likely arises because different potential shapes allow different kinds of orbits; specifically, x-tubes are more common in prolate potentials. We see this by plotting ξ_3 as a function of the fraction of x-tube orbits

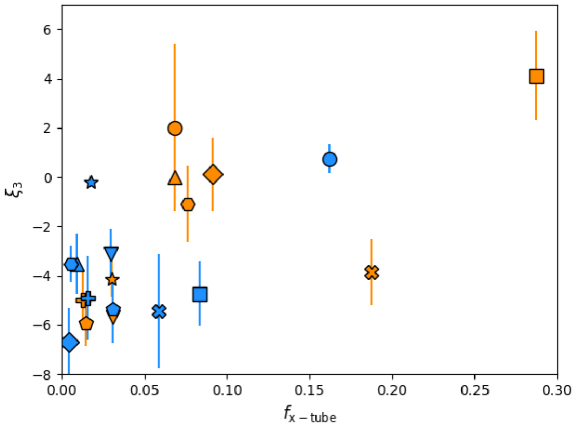

Figure 19. ξ_3 as a function of the fraction of x-tube orbits $f_{\rm x\text{-}tube}$ for our sample of simulated galaxies at $z = 0$. Colours and markers are the same as in Figs 17 and 18. The ξ_3 values of each galaxy are an average over 50 random views, and the error bars are their standard deviation. Galaxies with high $f_{\rm x\text{-}tube}$ tend to have $\xi_3 > 0$.

$f_{\rm x\text{-}tube}$ in Fig. 19. There is again a rough correlation, meaning that galaxies with higher $f_{\rm x\text{-}tube}$ are more likely to display a positive correlation between h_3 and $V_{\rm avg}/\sigma$ in their kinematic maps. This follows from the correlation between $f_{\rm x\text{-}tube}$ and the triaxiality T, which has previously been observed in isolated (Jesseit et al. 2005) and cosmological simulations (Röttgers et al. 2014). It should however be noted that in a pure prolate system only x-tube orbits and box orbits are allowed, and if there is net rotation around the long axis h_3 and $V_{\rm avg}/\sigma$ become anticorrelated again. We do not see this in our sample because none of our galaxies is dominated by x-tube orbits (at most $f_{\rm x\text{-}tube} = 0.25$, for 0227 *AGN*).

5.4 Isophotal shape

In Fig. 20 we plot the a_4/a parameter of all our galaxies versus their ellipticity ϵ at $z = 1$ and $z = 0$. Like for Figs 13 and 15, we also added contours to show the distribution of values for smaller inclinations. At $z = 1$ the panels with and without AGN feedback look qualitatively very similar. All galaxies have discy isophotes when viewed edge-on. When viewing the galaxies from different points of view both the ellipticity and the a_4/a values tend to become smaller. At $z = 0$, the cases with and without AGN behave as expected. The *NoAGN* galaxies show systematically higher a_4/a values, due to the formation of embedded stellar discs at low redshift. In the *AGN* case the a_4/a values are lower, meaning that the isophotes are less discy and closer to elliptical. Even though we do not have a clearly boxy galaxy in our sample, two galaxies (0175 and 0227) have almost perfectly elliptical isophotes.

We also computed the 3D shape of our galaxies using the triaxiality parameter T, defined in Section 3.3. The values of T for our galaxies are found in Table 1, or in Fig. 18. We found that with AGN feedback a bigger fraction of our galaxies (five out of ten, instead of two out of ten) has a triaxial or almost prolate shape ($T > 0.5$). A prolate shape is more common for massive ellipticals, as found in both observations (Tsatsi et al. 2017; Graham et al. 2018; Krajnović et al. 2018) and simulations (Li et al. 2018). Without AGN feedback more of our galaxies are oblate ($T \sim 0$) despite their larger mass, which makes them more similar to the significantly

Downloaded from https://academic.oup.com/mnras/article-abstract/489/2/2702/5556548 by Said Business School user on 05 November 2019

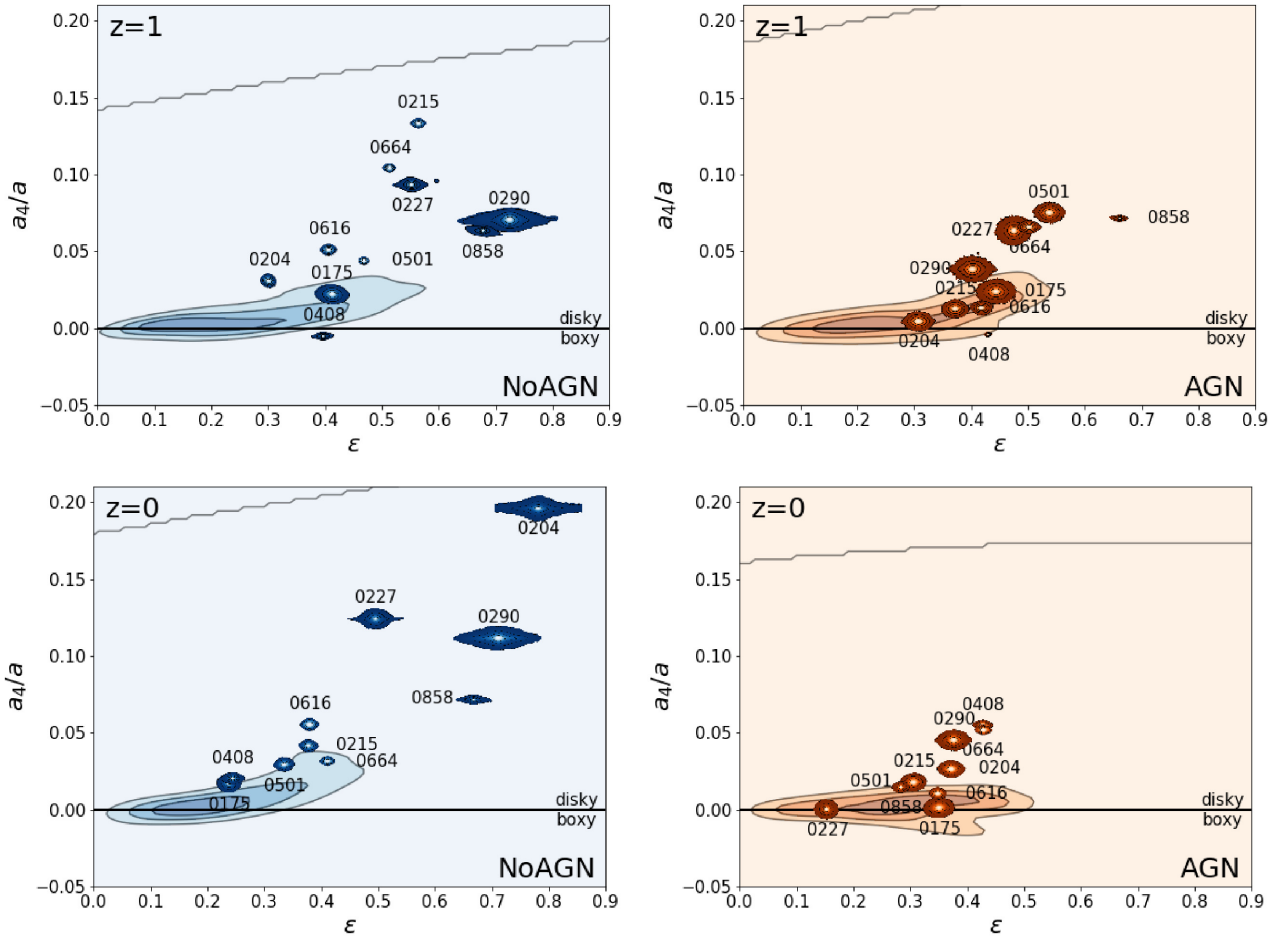

Figure 20. a_4/a versus galaxy ellipticity ϵ at $z = 1$ (top panels) and $z = 0$ (bottom panels), simulated without (left-hand panel) and with (right-hand panel) AGN feedback. The edge-on locations are indicated by the isophotal maps, while the density contours indicate the distribution of our galaxies when they are seen from 50 random orientations each. The black line indicates elliptical isophotes and separates boxy ($a_4 < 0$) from discy ($a_4 > 0$) galaxies. Galaxies with AGN feedback are rounder and have more elliptical – in one case even boxy – isophotes at $z = 0$.

less massive fast rotators we observe (Krajnović et al. 2011; Cappellari 2016).

5.5 Kinematic properties of the accreted component

The differences we analysed between the *AGN* and *NoAGN* simulations are most easily understood as a product of the prevention of late *in-situ* star formation by AGN feedback. As pointed out in Section 4.5 however, this is not the full story.

In the top panel of Fig. 21 we plot the λ_R parameter as a function of ellipticity ϵ, for our *AGN* and *NoAGN* sample, considering *only their accreted component*. This is achieved by filtering out all the particles which formed *in situ* since $z = 2$, prior to the kinematic analysis. The *AGN* galaxies have a similar distribution to the one of the full (accreted + *in situ*) systems (Fig. 13) and to what we expect from observational surveys. This is a consequence of these systems having formed in large part through accretion. The *NoAGN* galaxies are instead different from full counterparts having generally lower angular momentum and ellipticity. This is again expected, since the missing *in-situ* component is predominantly flatter and faster rotating. However, the accreted components of the *NoAGN* simulations are also different than the accreted *AGN* components; despite the lower λ_R values, they are in the range of fast rotators.

This effect is also visible in the ξ_3–λ_R plane: the accreted component of the *NoAGN* galaxies has different kinematics from the full galaxies and from their *AGN* counterpart, mostly lying in-between slow and fast rotators ($\lambda_R \sim 0.1$, $\xi_3 \sim -2$).

The fact that the accreted components of our two samples have different kinematics implies that the impact of AGN feedback is not limited to the suppression of *in-situ* star formation, but also affects the merger history of these galaxies, specifically making it more gas poor. Dryer mergers tend to further decrease the net angular momentum of galaxies and result in less oblate systems, which support a wider variety of orbits (most notably, x-tubes).

6 DISCUSSION AND CONCLUSIONS

From the analysis of these simulated galaxies emerges a clear picture, which confirms the previous studies on the subject and adds new insights. The energy output of AGNs heats up and pushes away the interstellar gas, effectively suppressing the *in-situ* formation of stars. This affects the kinematics and morphology of the systems with a stronger impact at later cosmic times, when the central black holes become more massive. In our simulations AGN feedback results in realistic early-type galaxy properties at $z = 0$. From our detailed stellar assembly, stellar population, mock IFU, isophotal shape, and stellar orbit analysis we get the following general picture:

Downloaded from https://academic.oup.com/mnras/article-abstract/489/2/2702/5556548 by Said Business School user on 05 November 2019

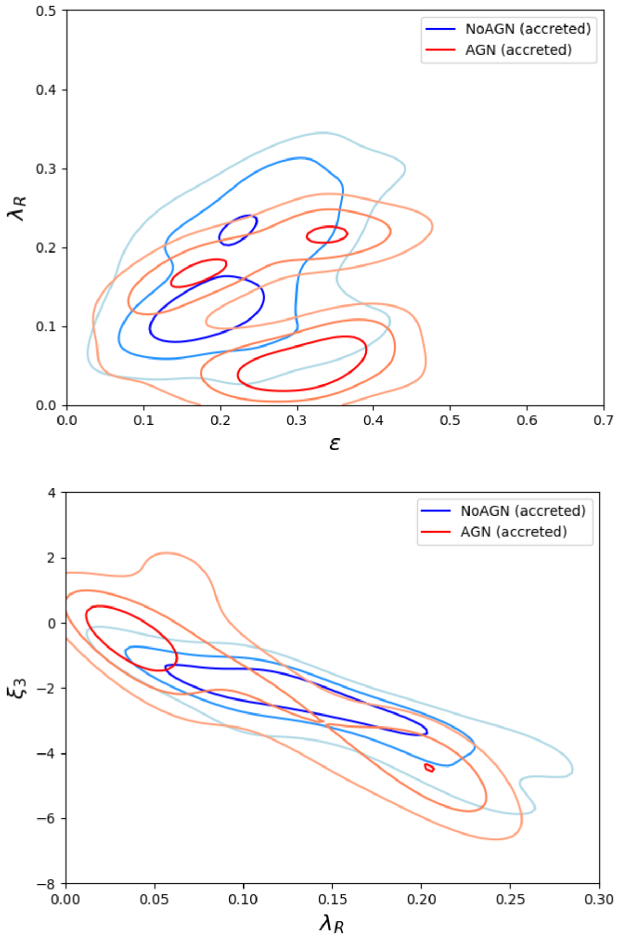

Figure 21. Top: Angular momentum proxy λ_R as a function of ellipticity ϵ, for our *NoAGN* (blue) and *AGN* (red) samples at $z = 0$, when considering only their accreted stellar component. Bottom: Same for ξ_3 versus λ_R. The fact that in both cases there is no overlap implies that the effect of AGN feedback on galaxy kinematics is not simply due to the prevention of late *in-situ* star formation.

(i) The stellar kinematics of massive early-type galaxies is significantly affected by AGN feedback, as seen both in the mock observational kinematic maps and in the orbit analysis of our simulation. Without AGN feedback massive early-type galaxies would develop young fast-rotating stellar discs even at low redshift, giving them kinematic signatures typical of less massive fast rotators. With AGN feedback massive early-type galaxies are instead more likely to become slow rotators due to the suppression of late *in-situ* star formation, in agreement with previous studies (Dubois et al. 2013; Martizzi et al. 2014; Penoyre et al. 2017b; Lagos et al. 2018).

(ii) As shown in Fig. 7, AGN feedback's effect of lowering the rotational support of galaxies is more pronounced in, but not limited to, late major mergers. Apart for some cases where mergers can cause a spin-up of the galaxy thanks to a favourable orbital configuration (Naab et al. 2014), most of the time mergers tend to disrupt the orbits of stars, reducing the angular momentum of the galaxy. However, without AGN feedback the further accretion of gas can produce a new rotating stellar disc and make the galaxy recover its angular momentum. With AGN feedback the in-falling star-forming gas is heated up and blown away. The origins of this mechanism lie in the different spatial and kinematic properties of *in-situ*-formed and accreted stars (Rodriguez-Gomez et al. 2016).

(iii) AGN feedback starts having a significant impact on the stellar angular momentum only after $z = 1$, and is stronger for more massive galaxies. With some exceptions, like galaxy 0616 in our sample which without AGN feedback develops a counter-rotating core, having AGN feedback always decreases the angular momentum of the galaxies in our sample.

(iv) While the main way that AGN feedback affects galaxy kinematics is by suppressing late *in-situ* star formation, its impact goes beyond that. By lowering the gas mass fraction of mergers it also affects the dynamics of the accreted stellar component.

(v) We compute the ellipticity ϵ and the a_4/a isophotal shape parameter and follow their evolution through cosmic time. By suppressing the formation of discs, AGN feedback makes galaxies less flattened and their isophotes significantly less discy (more elliptical or even boxy), especially when seen edge-on. Like for the angular momentum, this difference starts arising at $z \sim 1$, and its effect is again stronger for the most massive galaxies of our sample.

(vi) We introduce a new global parameter, the kinematic correlation ξ_3, to quantify the anticorrelation between the LOS-velocity and h_3 from 2D kinematic maps. Slow and fast rotators have different typical values of this parameter owing to their different orbital structures. AGN feedback pushes the ξ_3 value towards the slow-rotator regime ($\xi_3 \sim 0$, meaning a very steep anticorrelation between $V_{\rm avg}/\sigma$ and h_3 or lack of such a correlation).

(vii) We perform a full orbit analysis for all simulated galaxies and find that systems with AGN feedback have a higher fraction of x-tube and box orbits and a lower fraction of z-tubes. This is consistent with them being more triaxial due to the lack of late *in-situ* star formation and the more stellar accretion dominated assembly history. We find that the ξ_3 parameter is well correlated to the fractions of prolate z-tubes and x-tubes, as well as with the triaxiality of the galaxy.

(viii) We compared the ξ_3 values of our simulations with observed galaxies from the ATLAS^{3D} sample finding an interesting discrepancy. At equal λ_R, observed fast rotators seem to have values of ξ_3 closer to zero and sometimes even positive; this could be because many of these galaxies show bar features, which cause a positive correlation between h_3 and LOS velocity, and/or possibly because of noise in the observed h_3 values. Our *AGN* sample also lacks galaxies with high λ_R values, which are instead very common in the ATLAS^{3D} sample.

Even though slow-rotating galaxies could also form without AGN feedback through particularly gas-poor formation paths, our simulations suggest that AGN feedback might be essential to produce the observed amount of quiescent, slow-rotating and non-discy early-type galaxies. The impact of AGN on the rotation properties are in line with earlier studies using different AGN feedback models and simulation codes (Dubois et al. 2013; Martizzi et al. 2014; Penoyre et al. 2017b; Lagos et al. 2018). In this study we demonstrate that also higher order properties in the isophotal shape and line-of-sight kinematics, as well as the underlying orbital content, are significantly affected by accreting SMBH. The effects typically result in a better agreement with observations. The newly introduced kinematic correlation parameter ξ_3 might provide a useful diagnostic for large integral field surveys, as it is a kinematic indicator for intrinsic shape and orbital content. This study is not statistically complete nor can the assumed AGN feedback model

Downloaded from https://academic.oup.com/mnras/article-abstract/489/2/2702/5556548 by Said Business School user on 05 November 2019

be considered as an accurate description of the process. We can just give a model perspective on the observable effect of processes eventually happening in nature.

ACKNOWLEDGEMENTS

This research was supported by the German Federal Ministry of Education and Research (BMBF) within the German-South-African collaboration project 01DG15006 'Ein kosmologische Modell für die Entwicklung der Gasverteilung in Galaxien'. TN acknowledges support from the German Research Foundation (DFG) Excellence Cluster 'Universe'. MH acknowledges financial support from the European Research Council (ERC) via an Advanced Grant under grant agreement no. 321323-NEOGAL.

REFERENCES

Aumer M., White S. D. M., Naab T., Scannapieco C., 2013, MNRAS, 434, 3142
Aumer M., White S. D. M., Naab T., 2014, MNRAS, 441, 3679
Bacon R. et al., 2010, in McLean I. S., Ramsay S. K., Takami H., eds, Proc. SPIE Conf. Ser. Vol. 7735, Ground-based and Airborne Instrumentation for Astronomy III. SPIE, Bellingham, p. 773508 .
Bailin J., Steinmetz M., 2005, ApJ, 627, 647
Bender R., Moellenhoff C., 1987, A&A, 177, 71
Bender R., Saglia R. P., Gerhard O. E., 1994, MNRAS, 269, 785
Binney J., Tremaine S., 1987, Galactic Dynamics. Princeton University Press, Princeton.
Bois M. et al., 2010, MNRAS, 406, 2405
Bondi H., 1952, MNRAS, 112, 195
Bondi H., Hoyle F., 1944, MNRAS, 104, 273
Brennan R., Choi E., Somerville R. S., Hirschmann M., Naab T., Ostriker J. P., 2018, ApJ, 860, 14
Bruzual G., Charlot S., 2003, MNRAS, 344, 1000
Bryan S. E., Mao S., Kay S. T., Schaye J., Dalla Vecchia C., Booth C. M., 2012, MNRAS, 422, 1863
Bundy K. et al., 2015, ApJ, 798, 7
Cappellari M., 2016, ARA&A, 54, 597
Cappellari M., Copin Y., 2003, MNRAS, 342, 345
Cappellari M., Emsellem E., 2004, PASP, 116, 138
Cappellari M., Emsellem E., Krajnović D., McDermid R. M., Scott N., 2011a, MNRAS, 413, 813
Cappellari M. et al., 2011b, MNRAS, 413, 813
Carpintero D. D., Aguilar L. A., 1998, MNRAS, 298, 1
Choi E., Ostriker J. P., Naab T., Johansson P. H., 2012, ApJ, 754, 125
Choi E., Naab T., Ostriker J. P., Johansson P. H., Moster B. P., 2014, MNRAS, 442, 440
Choi E., Ostriker J. P., Naab T., Oser L., Moster B. P., 2015, MNRAS, 449, 4105
Choi E., Ostriker J. P., Naab T., Somerville R. S., Hirschmann M., Núñez A., Hu C.-Y., Oser L., 2017, ApJ, 844, 31
Choi E., Somerville R. S., Ostriker J. P., Naab T., Hirschmann M., 2018, ApJ, 866, 91
Chung A., Bureau M., 2004, AJ, 127, 3192
Crain R. A. et al., 2015, MNRAS, 450, 1937
Croom S. M. et al., 2012, MNRAS, 421, 872
Croton D. J. et al., 2006, MNRAS, 365, 11
de Kool M., Arav N., Becker R. H., Gregg M. D., White R. L., Laurent-Muehleisen S. A., Price T., Korista K. T., 2001, ApJ, 548, 609
Di Matteo T., Springel V., Hernquist L., 2005, Nature, 433, 604
Dressler A., 1989, in Osterbrock D. E., Miller J. S., eds, IAU Symposium Vol. 134, Active Galactic Nuclei. Kluwer, Dordrecht, p. 217
Dubois Y., Gavazzi R., Peirani S., Silk J., 2013, MNRAS, 433, 3297
Dubois Y., Peirani S., Pichon C., Devriendt J., Gavazzi R., Welker C., Volonteri M., 2016, MNRAS, 463, 3948
Eisenreich M., Naab T., Choi E., Ostriker J. P., Emsellem E., 2017, MNRAS, 468, 751
Emsellem E. et al., 2004, MNRAS, 352, 721
Emsellem E. et al., 2007, MNRAS, 379, 401
Emsellem E. et al., 2011, MNRAS, 414, 888
Emsellem E., Krajnović D., Sarzi M., 2014, MNRAS, 445, L79
Freedman D., Diaconis P., 1981, Z. Wahrscheinlichkeitstheor. Verwandte Geb., 57, 453
Gebhardt K. et al., 2000, ApJ, 539, L13
Gerhard O. E., 1993, MNRAS, 265, 213
Graham M. T. et al., 2018, MNRAS, 477, 4711
Guérou A., Emsellem E., Krajnović D., McDermid R. M., Contini T., Weilbacher P. M., 2016, A&A, 591, A143
Hernquist L., 1990, ApJ, 356, 359
Hernquist L., Ostriker J. P., 1992, ApJ, 386, 375
Hirschmann M., Naab T., Somerville R. S., Burkert A., Oser L., 2012, MNRAS, 419, 3200
Hirschmann M. et al., 2013, MNRAS, 436, 2929
Hirschmann M., Naab T., Ostriker J. P., Forbes D. A., Duc P.-A., Davé R., Oser L., Karabal E., 2015, MNRAS, 449, 528
Hirschmann M., Charlot S., Feltre A., Naab T., Choi E., Ostriker J. P., Somerville R. S., 2017, MNRAS, 472, 2468
Hoffman L., Cox T. J., Dutta S., Hernquist L., 2009, ApJ, 705, 920
Hoyle F., Lyttleton R. A., 1939, Proc. Camb. Phil. Soc., 35, 405
Hu C.-Y., Naab T., Walch S., Moster B. P., Oser L., 2014, MNRAS, 443, 1173
Iwamoto K., Brachwitz F., Nomoto K., Kishimoto N., Umeda H., Hix W. R., Thielemann F.-K., 1999, ApJS, 125, 439
Jedrzejewski R. I., 1987, MNRAS, 226, 747
Jesseit R., Naab T., Burkert A., 2005, MNRAS, 360, 1185
Jesseit R., Naab T., Peletier R. F., Burkert A., 2007, MNRAS, 376, 997
Jesseit R., Cappellari M., Naab T., Emsellem E., Burkert A., 2009, MNRAS, 397, 1202
Karakas A. I., 2010, MNRAS, 403, 1413
Kennicutt R. C., Jr, 1998, ApJ, 498, 541
Kormendy J., 1993, in Beckman J., Colina L., Netzer H., eds, The Nearest Active Galaxies. Consejo Superior de Investigaciones Cientificas, Madrid, p. 197
Kormendy J., Ho L. C., 2013, ARA&A, 51, 511
Krajnović D. et al., 2011, MNRAS, 414, 2923
Krajnović D., Emsellem E., den Brok M., Marino R. A., Schmidt K. B., Steinmetz M., Weilbacher P. M., 2018, MNRAS, 477, 5327
Kroupa P., 2001, MNRAS, 322, 231
Lagos C. del P., Schaye J., Bahé Y., Van de Sande J., Kay S. T., Barnes D., Davis T. A., Dalla Vecchia C., 2018, MNRAS, 476, 4327
Lauer T. R., 1985, MNRAS, 216, 429
Li H., Mao S., Emsellem E., Xu D., Springel V., Krajnović D., 2018, MNRAS, 473, 1489
Lilley E. J., Sanders J. L., Evans N. W., Erkal D., 2018, MNRAS, 476, 2092
Martizzi D., Jimmy, Teyssier R., Moore B., 2014, MNRAS, 443, 1500
McDermid R. M. et al., 2015, MNRAS, 448, 3484
Naab T., Burkert A., 2001, ApJ, 555, L91
Naab T., Burkert A., 2003, ApJ, 597, 893
Naab T., Ostriker J. P., 2017, ARA&A, 55, 59
Naab T., Burkert A., Hernquist L., 1999, ApJ, 523, L133
Naab T., Jesseit R., Burkert A., 2006, MNRAS, 372, 839
Naab T., Johansson P. H., Ostriker J. P., 2009, ApJ, 699, L178
Naab T. et al., 2014, MNRAS, 444, 3357
Núñez A., Ostriker J. P., Naab T., Oser L., Hu C.-Y., Choi E., 2017, ApJ, 836, 204
Oser L., Ostriker J. P., Naab T., Johansson P. H., Burkert A., 2010, ApJ, 725, 2312
Oser L., Naab T., Ostriker J. P., Johansson P. H., 2012, ApJ, 744, 63
Ostriker J. P., Choi E., Ciotti L., Novak G. S., Proga D., 2010, ApJ, 722, 642
Penoyre Z., Moster B. P., Sijacki D., Genel S., 2017a, MNRAS, 468, 3883
Penoyre Z., Moster B. P., Sijacki D., Genel S., 2017b, MNRAS, 468, 3883

Downloaded from https://academic.oup.com/mnras/article-abstract/489/2/2702/5556548 by Said Business School user on 05 November 2019

Robertson B., Yoshida N., Springel V., Hernquist L., 2004, ApJ, 606, 32
Rodriguez-Gomez V. et al., 2016, MNRAS, 458, 2371
Röttgers B., Naab T., Oser L., 2014, MNRAS, 445, 1065
Sánchez S. F. et al., 2012, A&A, 538, A8
Sazonov S. Y., Ostriker J. P., Ciotti L., Sunyaev R. A., 2005, MNRAS, 358, 168
Scannapieco C., Tissera P. B., White S. D. M., Springel V., 2005, MNRAS, 364, 552
Scannapieco C., Tissera P. B., White S. D. M., Springel V., 2006, MNRAS, 371, 1125
Schaye J. et al., 2015, MNRAS, 446, 521
Schulze F., Remus R.-S., Dolag K., Burkert A., Emsellem E., van de Ven G., 2018, MNRAS, 480, 4636
Somerville R. S., Davé R., 2015, ARA&A, 53, 51
Spergel D. N. et al., 2007, ApJS, 170, 377
Springel V., 2000, MNRAS, 312, 859
Springel V., 2005, MNRAS, 364, 1105
Stewart G. W., 1980, SIAM J. Numer. Anal., 17, 403
Thomas J., Saglia R. P., Bender R., Thomas D., Gebhardt K., Magorrian J., Corsini E. M., Wegner G., 2007, MNRAS, 382, 657
Tsatsi A., Lyubenova M., van de Ven G., Chang J., Aguerri J. A. L., Falcón-Barroso J., Macciò A. V., 2017, A&A, 606, A62
van de Sande J. et al., 2017, ApJ, 835, 104
van der Marel R. P., Franx M., 1993, ApJ, 407, 525
Vasiliev E., 2013, MNRAS, 434, 3174
Veale M. et al., 2017, MNRAS, 464, 356
Vogelsberger M. et al., 2014, Nature, 509, 177
Woosley S. E., Weaver T. A., 1995, ApJS, 101, 181
Wu X., Gerhard O., Naab T., Oser L., Martinez-Valpuesta I., Hilz M., Churazov E., Lyskova N., 2014, MNRAS, 438, 2701

APPENDIX: ADDITIONAL FIGURES

Figs A1 and A2 show the kinematic maps of galaxy 0227 at $z = 0$ separating the stars between different age groups: younger than 3 Gyr (formed after the major merger at $z = 0.25$), between 3 and 10 Gyr old, and older than 10 Gyr. In the case with AGN feedback the galaxy has too few stars belonging to the first group, so we skipped it. Without AGN feedback there are instead many stars in this group, and they are almost all on rotational orbits in a thin disc, with few stars above or below its plane. This disc rotates very fast, at around 400 km s^{-1}, has very little velocity dispersion and shows quite extreme signatures in the h_3 and h_4 maps. Interestingly the intermediate age group shows an extended velocity dispersion signature, perhaps due to the presence of several non-aligned remnants of discs that were also quenched in the case with AGN feedback. The older stars behave in a relatively similar way with or without AGN feedback. Their rotational velocity is smaller and their dispersion much higher, similar to the maps for the accreted component (Top panel of Fig. 11). From the youngest to the oldest age group, the value of the λ_R parameter is 0.84, 0.38, and 0.35 for the case without AGN, and 0.10 and 0.13 for the case with AGN. The old stars rotate faster in the case without AGN, likely because of the dee per central potential.

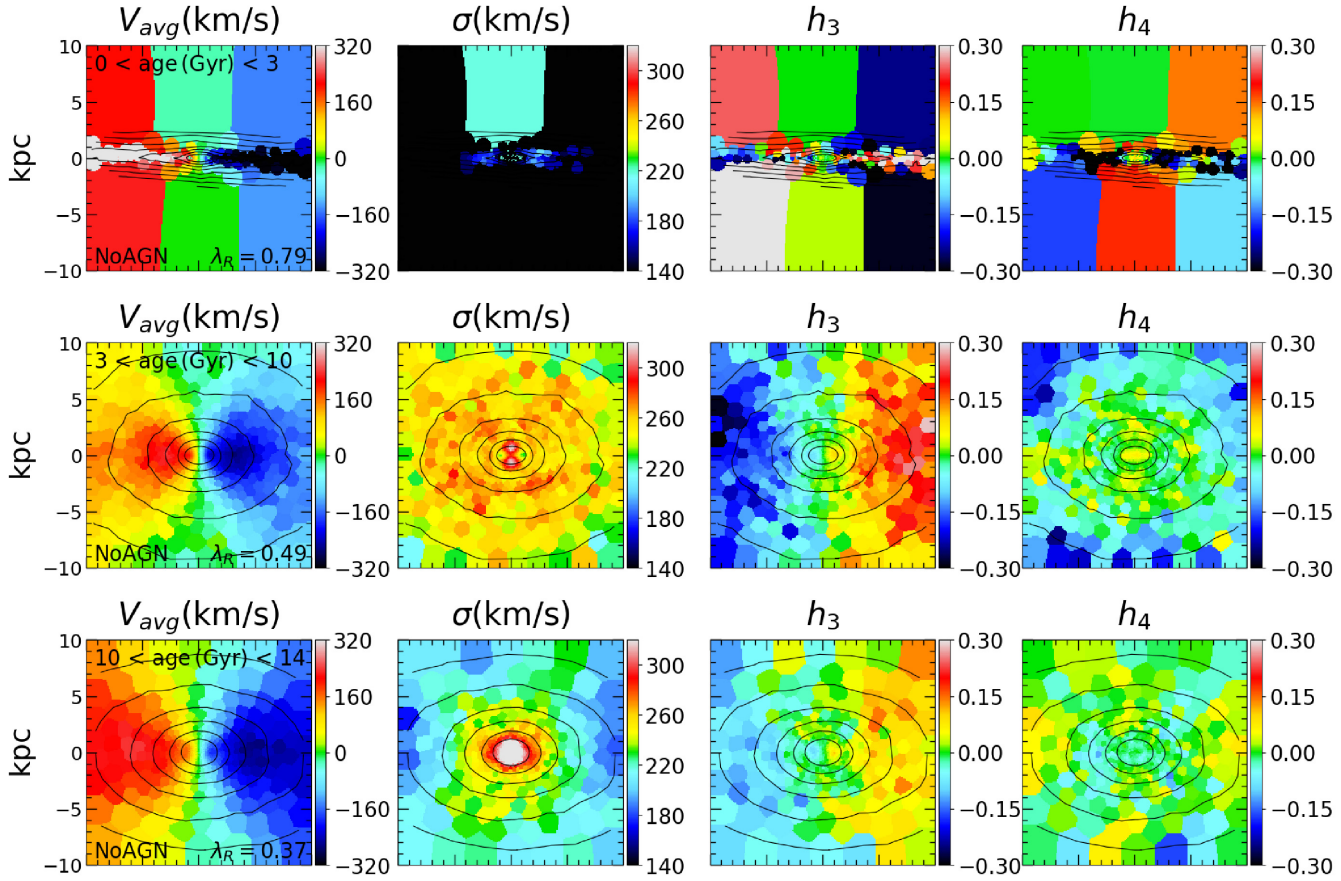

Figure A1. Kinematic maps (V_{avg},σ,h_3,h_4) for age-selected stellar components of galaxy 0227 simulated without AGN. From top to bottom, stars between 0 and 3 Gyr old, between 3 and 10 Gyr old, and older than 10 Gyr.

Downloaded from https://academic.oup.com/mnras/article-abstract/489/2/2702/5556548 by Said Business School user on 05 November 2019

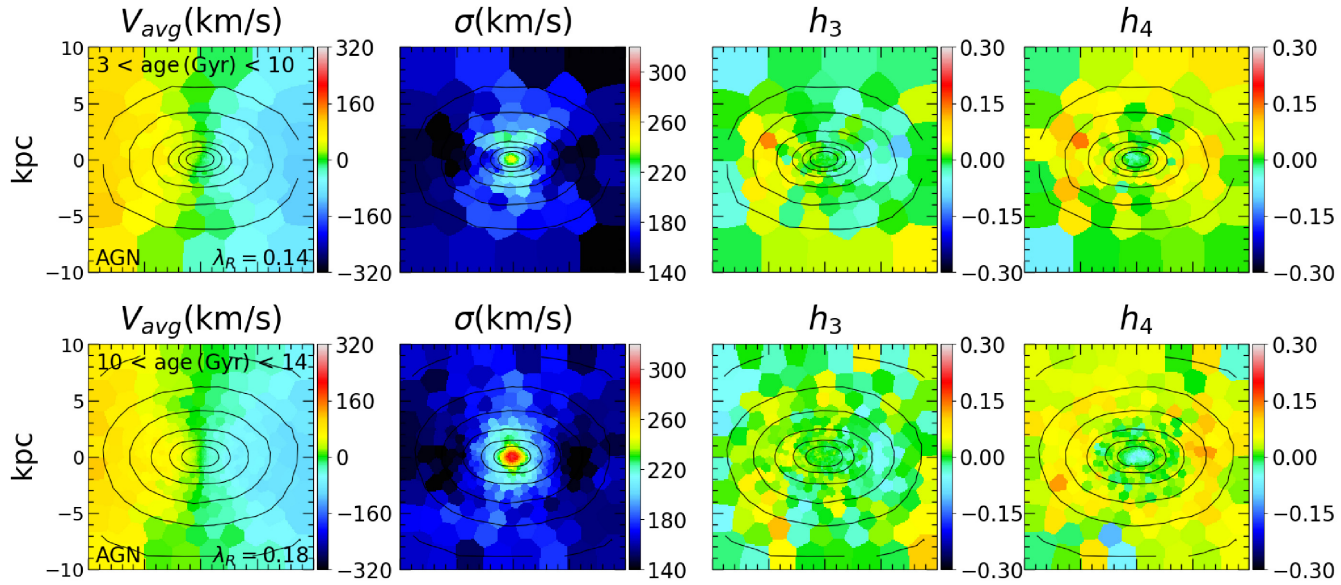

Figure A2. Kinematic maps (V_{avg},σ,h_3,h_4) for age-selected stellar components of galaxy 0227 simulated with AGN. From top to bottom, stars between 0 and 10 Gyr old and stars older than 10 Gyr.

This paper has been typeset from a TEX/LATEX file prepared by the author.

Downloaded from https://academic.oup.com/mnras/article-abstract/489/2/2702/5556548 by Said Business School user on 05 November 2019